# Development of Tollmien-Schlichting disturbances in the presence of laminar separation bubbles on an unswept infinite wavy wing

Christian Thomas and Shahid Mughal
*Department of Mathematics, South Kensington Campus,*
*Imperial College London, London, SW7 2AZ, UK**

Richard Ashworth
*Airbus Group Innovations, Bristol, BS99 7AR, UK*

The effect of long wavelength sinusoidal surface waviness on the development of Tollmien-Schlichting (TS) wave instabilities is investigated. The analysis is based on the compressible flow that forms over an unswept infinite wavy wing with surface variations of variable amplitude, wavelength and phase. Boundary layer profiles are extracted directly from the solutions of a Navier-Stokes solver, which allows a thorough parametric analysis to be undertaken. Many wavy surface configurations are examined that can be sufficient to establish localised pockets of separated flow. Linear stability analysis is undertaken using parabolised stability equations (PSE) and linearised Navier-Stokes (LNS) methods, and surface waviness is generally found to enhance unstable behaviour. Results of the two schemes are compared and criteria for PSE to establish accurate solutions in separated flows are determined, which are based on the number of TS waves per wavelength of the surface deformation. Relationships are formulated, relating the stability variations and the surface parameters, which are consistent with previous observations regarding the growth of TS waves on a flat plate. Additionally, some long wavelength surface deformations are found to stabilise TS disturbances.

* c.thomas@imperial.ac.uk

## I. INTRODUCTION

Accurate prediction of boundary layer transition on aerofoils is critical to the improvement of future wing design. Surface deformations that have been established by environmental conditions (roughness or hail stone impacts [1]) or industrial effects (steps, gaps and waviness) can potentially cause significant variations in the onset of transition, which may have a severe impact on the flight performance characteristics. Several studies have examined the effect of short-scale surface deformations (as listed in table I), while for the current investigation we explore the effect of long wavelength variations on an unswept infinite wing.

Wind tunnel experiments carried out by Fage [2] examined the effect of various surface deformations (bulges, hollows, ridges) on transition to turbulence. Experiments were conducted on both a flat plate with a small favourable pressure gradient and an aerofoil. Using his observations, Fage derived the following relationship

$$\frac{h^2 x_{tr}^2 Re_\infty^3}{\lambda} = 8.1 \times 10^{13}; \quad \sqrt{\lambda l}/x_{tr} < 0.09, \tag{1}$$

to describe the minimum height $h$ required to affect the onset of boundary layer transition. Here $\lambda$ and $l$ denote the respective length and location of the deformation, $x_{tr}$ is the chord location for transition and $Re_\infty$ represents the freestream Reynolds number. Further experiments by the Carmichael group [3–5] included both compressible and pressure gradient effects on a wavy wing body. Using the experimental flight data Carmichael formulated the expression

$$\frac{h^2 c^{1/2} Re_\infty^{3/2}}{\lambda} = 51300, \tag{2}$$

that defines the critical size of the surface waviness for a two-dimensional (2D) flow.

Holmes and collaborators [6, 7] reported on manufacturing tolerances and flight experiments that included various step, gap and surface wave imperfections. It was found that the Tollmien-Schlichting (TS) wave instability was significantly destabilised in the region of the surface wave that generates an adverse pressure gradient. Additionally, increasing the height of step deformations on a 2D flat plate significantly augments the growth of the TS wave and brings about the premature onset of transition [8].

The effect of wall waviness on the stability of the incompressible Blasius boundary layer was considered by Lessen and Gangwani [9], who found that the critical Reynolds number for transition decreased with the height of the wave. Using solutions of the compressible boundary layer equations, Lekoudis *et al.* [10] computed the effect of shallow surface waves on the meanflow and obtained good agreement with the earlier experimental observations. However, for surface variations that were sufficiently large to establish separation, the boundary layer method for generating the basic state breaks down. This failing of the boundary layer computations is a direct consequence of the streamwise marching numerical procedure [11]; thus limiting boundary layer and stability analysis for some forms of surface deformations. However, such difficulties can be overcome by the implementation of alternative methods, including the interactive boundary layer (IBL) procedure that allows the boundary layer equations to be solved even for separated flows [12].

Several theoretical investigations considered the effect of a hump on a 2D flat plate without a streamwise pressure gradient [13–15]. In these particular studies the undisturbed basic state was established using the IBL procedure, while linear stability analysis was performed using a parallel flow approximation where the streamwise variation of the meanflow was ignored. A locally based $e^N$ method [16–19] was utilised to predict the onset of boundary layer transition and the theoretical findings were qualitatively similar to the observations of Fage [2].

The IBL methods were further utilised by Wie and Malik [20] to compute a subsonic 2D base flow over a flat-plate with wavy surface variations. The effect of waviness on the growth of the linear TS wave instability was carried out using parabolised stability equation (PSE) methods [21], which were based on a non-parallel boundary layer that took into account the streamwise variations of the undisturbed flow. Several surface wave configurations and freestream conditions were considered and it was determined that wavy deformations could establish significant increases in the amplification rate of the disturbance. Additionally, Wie and Malik were able to derive an expression relating the variation of the $N$-factor amplification rate

$$\Delta N = N_{\text{Wavy}} - N_{\text{Non-Wavy}},$$

and the physical dimensions of the surface wave for the flow over a flat-plate with a favourable pressure gradient:

$$\Delta N = 0.07 \frac{n h^2 Re_\infty}{\lambda}, \tag{3}$$

| Reference | Study Type | Geometry | Deformation Type |
|---|---|---|---|
| Fage [2] | Experimental | Flat Plate/Aerofoil | Bulges/Hollows/Ridges |
| Carmichael Group [3–5] | Experimental | Aerofoil | Waviness |
| Holmes Group [6, 7] | Experimental | Aerofoil | Steps/Gaps |
| Wang & Gaster [8] | Experimental | Flat Plate | Steps |
| Lessen & Gangwani [9] | Theoretical | Flat Plate | Waviness |
| Nayfeh *et al* [13] | Theoretical | Flat Plate | Humps |
| Cebeci & Egan [14] | Theoretical | Flat Plate | Humps |
| Masad & Iyer [15] | Theoretical | Flat Plate | Humps |
| Wie & Malik [20] | Theoretical | Flat Plate | Waviness |
| Park Group [23, 24] | Theoretical | Flat Plate | Humps |
| Brehm *et al* [25] | Theoretical | Flat Plate | Ridges/Roughness |
| Gaster [26] | Experimental | Flat Plate | Ridges/Roughness |

TABLE I. Type of surface deformations investigated by previous investigators.

where the parameter $n$ defines the number of waves before the onset of transition $x_{tr}$ (given for the non-deformed model). Comparing their expression for the allowable measure of surface waviness with that formulated by Fage and Carmichael [2, 4], Wie and Malik concluded that Fage's criteria (1) was quite restrictive and allows significantly smaller waviness than the relationship conceived by Carmichael (2). It was suggested that expression (3) could be used to estimate the effect on stability and transition for a limited range of surface dimensions, provided that surface waviness did not enhance receptivity or excite nonlinear interaction with centrifugal instabilities that may develop as a result of the surface waviness [22].

PSE methods were also employed by Park and collaborators [23, 24] to investigate the effects of a hump on both the linear and nonlinear development of the TS wave instability. Both the height and length scales of the hump were again critical to the amplification rate of the disturbances. Nonlinear interaction was found to greatly amplify the size of the perturbation and it was concluded that this may cause the premature breakdown of the laminar flow.

Thomas *et al.* [27] considered the effect of surface waviness on the crossflow instability that develops in a compressible flow on an infinite swept wing body. Their study was based on the flow solutions of an industrial Reynolds-Averaged Navier-Stokes (RANS) formulation called TAU [28], where laminar flow was established by specifying the onset of transition; the RANS scheme solves the laminar form of the Navier-Stokes equations. Boundary layer solutions in this limit were then extracted directly from the TAU output and formatted for a stability analysis based on both PSE and linearized Navier-Stokes (LNS) methods [29, 30]. Similar extraction methods have been developed by Malik and co-workers [31, 32] for investigating the stability of the flow on flat plates and full aircraft configurations. Thomas and collaborators [27] validated their 'RANS extracted boundary layer' (REBL) solutions against results of a compressible boundary layer formulation [33] that applies a streamwise marching strategy [11]. As boundary layer profiles were drawn directly from the TAU solutions, a thorough stability investigation was undertaken for several surface configurations, including those wavy dimensions that established separation. It was shown that, depending on the location used to draw comparisons, surface waviness of variable height, wavelength and phase could marginally stabilise and destabilise the crossflow instability. Furthermore, utilising the $e^N$ method for estimating transition, Thomas *et al.* found that surface waviness could generate variations in the chord location where laminar-turbulent transition was established. However, stability variations $\Delta N$ were small compared with the observations of Wie and Malik [20] on TS disturbances. Additionally, PSE solutions were in excellent agreement with the corresponding LNS computations, with only minor differences arising for those flow systems containing small pockets of separation.

Recently, Brehm *et al* [25] undertook a theoretical investigation of 2D distributed wall roughness effects on a flat plate, with the aim of corroborating the experimental findings of Gaster [34]. In their study they found that roughness modelled as 2D rectangular or sinusoidal elements could establish separated flow. Their numerical results confirmed Gaster's observations that there exists a critical roughness height, beyond which the amplification of the TS wave instability increases with increasing height. The effect of sinusoidal roughness distributions on the growth of the TS wave was also considered by Gaster [26], who used the Orr-Sommerfeld equation to obtain solutions to the basic state and undertake a perturbation analysis. Separated flow was found to form between sufficiently large roughness elements, while the amplification rate of the perturbations was enhanced by the roughness.

In the following investigation, PSE and LNS methods are utilised to study the effect of long wavelength surface waviness on the growth of the TS wave instability. This expands upon the earlier theoretical studies that considered short-scale deformations on a flat plate (refer to table I). The undisturbed flow on an unswept infinite wing of variable surface waviness is established using the TAU industrial flow solver, where the surface variations can establish localised pockets of separation. The suitability of the PSE approach for investigating disturbances in separated flows

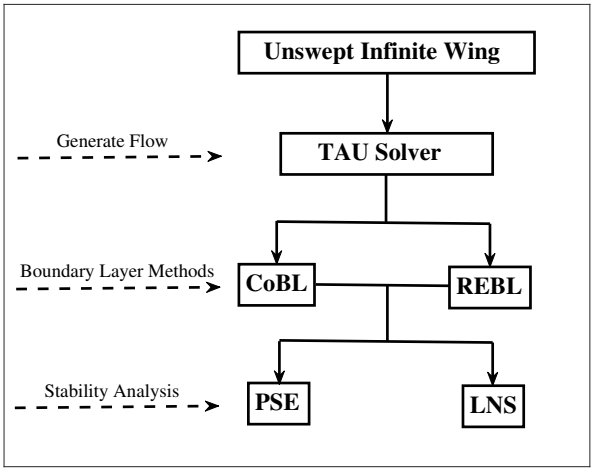


FIG. 1. Flow chart diagram illustrating the methodology for the boundary layer and stability analysis. CoBL - Compressible Boundary Layer; REBL - RANS Extracted Boundary Layer; PSE - Parabolised Stability Equations; LNS - Linearised Navier-Stokes.

is a contentious issue. PSE methods are based on a streamwise marching procedure that do not account for the upstream propagation associated with boundary layer separation. Furthermore, separated flow can establish absolute instability, for which PSE methods are most definitely not applicable. Hammond and Redekopp [35] suggest that absolutely unstable behaviour will develop in laminar separation bubbles if the peak value of the reverse flow reaches about 30% of the freestream magnitude, while Adam and Sandham [36] indicate that more than 15% reverse flow is required for the onset of absolute instability.

On the applicability of the PSE approach for studying convective disturbances in systems with reverse flow, Wie and Malik suggest that the PSE method may be able to successfully 'step-over' a small separation bubble. This particular conclusion was drawn, based on the minimum step-size restriction derived by Li and Malik [37]; $\Delta x > 1/|\alpha_r|$ for a stable solution. Here $\alpha_r$ and $\Delta x$ represent the real part of the streamwise wavenumber and the associated step-size. Li and Malik also proposed a Parabolised Navier-Stokes type strategy [38], whereby the streamwise pressure gradient term is suppressed, leading to a relaxation of the step-size limit. However, Andersson *et al* [39] introduce a stabilisation procedure that allows the pressure gradient term to be retained in the PSE formulation allowing numerically stable solutions to be obtained for considerably smaller step-sizes than that established by the Li-Malik step-size criteria. Furthermore, there are some indications from within the available literature that the PSE approach may be used to calculate disturbances in separated flow systems to an acceptable degree of accuracy. For instance, Gao *et al* [23] compared solutions of their PSE analysis with that established via direct numerical simulations, and found that the PSE method can work well in flow systems with a small amount of boundary layer separation. Additionally, Wie and Malik [20] state (though do not publish) that they successfully applied the PSE method through separation bubbles.

The remainder of this paper is outlined as follows. In the subsequent section we describe the routines for generating the basic state on a wavy wing, and the PSE and LNS methods used to undertake a linear stability analysis of TS disturbances. Boundary layer solutions are presented in §III for both non-separated and separated flow systems, while results of both the PSE and LNS methods are discussed in §IV. PSE and LNS results are compared and we examine the criteria necessary for PSE to establish solutions to a reasonable degree of accuracy in separated flows. Finally, we conclude our investigation with several comments pertaining to the observations of our study.

## II. FORMULATION

Compressible flow characteristics and boundary layer disturbances that develop on a wavy wing are determined using several numerical schemes. Accurate and robust methods are required to successfully capture the effect of surface waviness on the evolution of TS wave instabilities. In this section we discuss and highlight the essential ingredients, as depicted in figure 1, for generating solutions and achieving the objectives of this investigation.

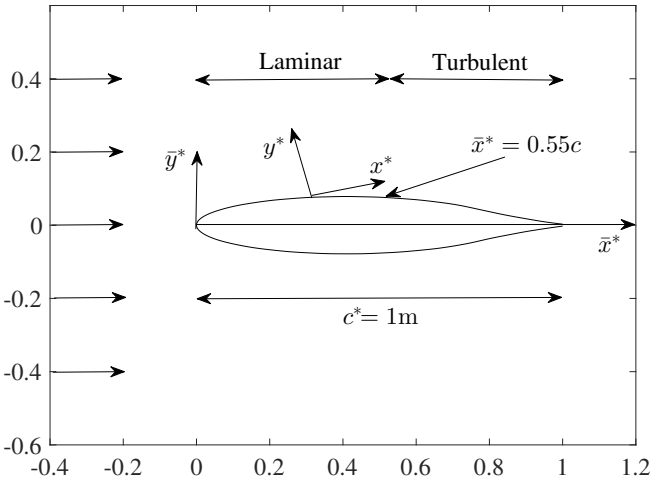


FIG. 2. Cross-sectional view of the unswept infinite wing model.

### A. Wing Model

#### 1. Non-Deformed Geometry

Figure 2 depicts a cross-sectional view of the wing geometry, used in this investigation, in 2D Cartesian coordinates $\bar{\boldsymbol{x}}^* = \{\bar{x}^*, \bar{y}^*\}$ [40] (asterisks denote dimensional properties). As our interest is in flow variations along the $\bar{x}^*$-direction and 2D TS wave instabilities, the wing model and the resulting flow dynamics are assumed to be independent of a third spanwise axis. Additionally, the angle of incidence is set equal to zero. Although the wing geometry represents a simple aerofoil, it is reasonable to assume that the stability analysis illustrated in this paper will also appear (in one form or other) on other wing geometries with comparable surface features and freestream characteristics. The chord length of the model $c^* = 1$m, whilst the maximum thickness is approximately 0.15m near the chord centre. The flow is assumed to be compressible with a Mach number $M_\infty$ and a freestream Reynolds number $Re_\infty$ based on the chord $c^*$. Finally, the freestream temperature $T_\infty = 300$K for all flow conditions considered.

#### 2. Imposing Surface Waviness

The surface of the wing is deformed using sinusoidal wave variations of the form

$$s = H^* \sin\{2\pi x^*/\lambda^* - \phi\} \quad \text{on} \quad y^* = 0, \tag{4}$$

where $x^*$ represents the chordwise surface axis and $y^*$ is the wall-normal direction (as depicted in figure 2). Here $H^*$ is the amplitude (or half height) and $\lambda^*$ is the wavelength of the wavy surface, which are both scaled on the chord length $c^*$. Note that in all future discussion $H = H^*/c^*$ and $\lambda = \lambda^*/c^*$ are used to define the surface variations. The parameter $\phi$ is a phase shift, which when set to zero establishes a surface wave originating at the attachment-line $\bar{x}^* = x^* = 0$.

In subsequent sections we limit our analysis to surface configurations $\lambda \in [0.1 : 0.1 : 0.4]$, $H \in [0 : 0.0001 : 0.0006]$ and four equally spaced phase shifts $\phi \in [-\pi/2 : \pi/2 : \pi]$. Smaller wavelengths were not considered as significantly denser meshes would have been required to establish accurate flow solutions (see §II A 3), while the amplitudes $H$ are relatively large and correspond to deformations of order one tenth of a millimetre. This particular characteristic was implemented to ensure variations in the flow dynamics were sufficient enough to establish localised pockets of separation.

### 3. Generating Flow Solutions

The steady flow, about the wavy wing, was generated using the TAU industrial flow solver [28]. The TAU program solves the RANS system of equations for the flow that develops about 2D and 3D geometries. For the current investigation the method was made applicable to the analysis of laminar flows by imposing a fixed transition line (as depicted in figure 2) at $x^* = 0.55c^*$. This was implemented to avoid convergence issues that could arise with the formation of severe separation along the trailing edge of a laminar wing. Although pockets of separated flow were established within the troughs of some of the wavy surface geometries considered herein, they were relatively small. Thus, laminar flow was established for $x^* \leq 0.55c^*$ by setting the eddy viscosity in the TAU formulation to zero; the RANS scheme thus reduces to solving the laminar Navier-Stokes equations. Downstream of the transition location, the full RANS formulation was solved and a fully turbulent boundary layer was allowed to develop. However, in the subsequent sections, the analysis of TS disturbances was restricted to the laminar flow domain.

A sufficiently dense unstructured mesh was established (about the wavy wing) to ensure accurate flow features were captured by the TAU formulation. After careful experimentation it was determined that at least 40 mesh points were required within the boundary layer region, to ensure that the flow dynamics were fully captured. Beyond the boundary layer, the mesh density was significantly reduced and quite sparse in the far field limit (which was set at about 50 chord lengths $c^*$ from the wing). Along the length of the wing, approximately 500 mesh points were required to generate accurate flow solutions. Decreasing the minimum wavelength $\lambda$ beyond that considered herein would have required this latter mesh specification to be greatly increased, leading to larger computational requirements.

Given a set of freestream flow conditions $\{M_\infty, Re_\infty\}$ the TAU solver simulates the dimensional steady flow $\bar{\boldsymbol{Q}}^*_B = \{\bar{\boldsymbol{U}}^*_B, \bar{P}^*_B, \bar{T}^*_B\}$ in Cartesian coordinates $\bar{\boldsymbol{x}}^*$. The vector $\bar{\boldsymbol{U}}^*_B$ denotes the undisturbed dimensional velocity field, while $\bar{P}^*_B$ and $\bar{T}^*_B$ respectively represent the pressure and temperature variables. A converged steady-state solution was then obtained by using the Spalart-Allmaras-Edwards turbulence model [41]. Flow solutions were obtained subject to satisfying no-slip conditions on the wing surface and far-field boundary conditions given by the freestream specification. An explicit Runge-Kutta iterative scheme was then utilised, where it was assumed that a steady basic state was achieved once residuals were of the order $10^{-8}$ and less.

## B. Boundary Layer Methods

A non-dimensional steady basic state $\boldsymbol{Q}_B = \{\boldsymbol{U}_B, P_B, T_B\}(\boldsymbol{x})$ (in non-dimensional surface coordinates $\boldsymbol{x} = \{x, y\}$) was required to conduct both a PSE and LNS investigation of TS wave instabilities. Boundary layer profiles were obtained by either solving a set of boundary layer equations or by carefully extracting profiles directly from the TAU solutions. The former method is based on the results of the infinitely swept boundary layer equations (CoBL [33]), where a surface pressure distribution is required as an initial input taken directly from the TAU output. These particular equations were discretised using a fully implicit second-order accurate three-point backward differencing scheme along the chordwise axis, whilst a two point second-order accurate method was utilised in the wall-normal direction.

A second boundary layer method, REBL [27], is based entirely on the output generated by the TAU flow solver. The REBL scheme extracts the dimensional TAU solutions and transforms the results from the dimensional Cartesian coordinates $\bar{\boldsymbol{x}}^*$ to the non-dimensional surface fitted coordinate system $\boldsymbol{x} = \{x, y\}$. The extraction procedure was achieved by implementing several geometric transformations and boundary-layer properties. Paraview filters [42] were used that perform several processes during the boundary-layer extraction process, while arithmetic operations were performed using Python to the default 15 decimal place accuracy. Firstly, unit normals $\bar{\boldsymbol{x}}^*_n = \{\bar{x}^*_n, \bar{y}^*_n\}$ were generated at all points along the wing surface. Dimensional flow profiles were then extracted along each normal and transformed using the matrix operator

$$\mathcal{A} = \begin{bmatrix} \bar{y}^*_n & \bar{x}^*_n \\ -\bar{x}^*_n & \bar{y}^*_n \end{bmatrix},$$

to give

$$\boldsymbol{x}^* = \mathcal{A}\bar{\boldsymbol{x}}^* \quad \text{and} \quad \boldsymbol{U}^*_B = \mathcal{A}\bar{\boldsymbol{U}}^*_B,$$

where the dimensional vector $\boldsymbol{U}^*_B = \{U^*_B, V^*_B\}$ represents the 2D undisturbed velocity field in surface fitted coordinates $\boldsymbol{x}^*$, while $P^*_B = \bar{P}^*_B$ and $T^*_B = \bar{T}^*_B$. Non-dimensional quantities were then obtained by scaling flow properties on their boundary layer edge values, based on the location where the $U^*_B$-velocity field attains 99% of its maximum. Thus, the non-dimensional velocity field

$$\boldsymbol{U}_B = \frac{\boldsymbol{U}^*_B}{U^*_e},$$

where the subscript $e$ denotes the boundary layer edge characteristics. Hence, at each chord location $U_B \to 1$ as $y \to \infty$. Similar representations were formulated for the non-dimensional pressure $P_B = P_B^*/P_e^*$ and temperature $T_B = T_B^*/T_e^*$.

For the subsequent discussion of the PSE and LNS formulation, non-dimensional coordinates $\boldsymbol{x}$ were obtained by scaling on a locally defined boundary layer thickness $\delta^*$ that was measured about a fixed location:

$$\boldsymbol{x} = \boldsymbol{x}^*/\delta^*.$$

However, in §III and IV, the base flow and stability calculations are presented in terms of a coordinate system scaled on the chord length $c^*$; $\boldsymbol{x} = \boldsymbol{x}^*/c^*$. Note that the same character has been used to represent non-dimensional coordinates based on $\delta^*$ and $c^*$, which has been implemented to avoid introducing further notation. Additionally, results are presented in $\boldsymbol{x} = \boldsymbol{x}^*/c^*$ coordinates as this provides a better means of illustrating the flow dynamics.

### C. Stability Methods

The stability of the undisturbed flow $\boldsymbol{Q}_B$ was undertaken by considering infinitesimally small time periodic perturbations

$$\boldsymbol{q}'(x, y, t) = \boldsymbol{q}(x, y) \exp\{-i\omega t\},$$

where $\boldsymbol{q} = \{u, v, p, T\}$ and $\omega$ represents a local non-dimensional frequency given as

$$\omega = \frac{2\pi f^* \delta^*}{U_e^*}.$$

The parameter $f^*$ is the dimensional frequency of the perturbation that is measured per unit hertz (Hz). For presentation purposes we introduce a non-dimensional global frequency

$$f = \frac{2\pi f^* \nu_\infty^*}{U_\infty^{*2}}, \tag{5}$$

where $U_\infty^*$ and $\nu_\infty^*$ respectively denote the freestream velocity and kinematic viscosity.

#### 1. *PSE Theory*

Linear PSE perturbations $\boldsymbol{q}$ are decomposed as

$$\boldsymbol{q} = \tilde{\boldsymbol{q}}(x, y) E(x) + \text{c.c}, \tag{6}$$

where $\tilde{\boldsymbol{q}}$ represents a slowly varying in $x$ amplitude function and $E$ is a wave function of the form

$$E(x) = \exp\left\{ i \int_{x_0}^{x} \alpha(\zeta)\, \mathrm{d}\zeta \right\}. \tag{7}$$

The real and imaginary parts of $\alpha$ respectively denote the wavenumber and growth rate of the TS disturbance, while $x_0$ represents the critical location for the onset of the instability.

The linear PSE formula for the shape function $\tilde{\boldsymbol{q}}$ is represented as

$$L\tilde{\boldsymbol{q}} + M\frac{\partial \tilde{\boldsymbol{q}}}{\partial x} = 0, \tag{8}$$

where $L$ and $M$ are differential matrix operators in the wall-normal $y$-direction (a detailed description of the matrix operators are given in Mughal [43]). Both $L$ and $M$ are dependent on the curvature of the surface that are embodied in the terms $\kappa$ and $\chi$ that respectively represent the local body curvature and

$$\chi = \frac{1}{1 - \kappa y}. \tag{9}$$

The system of equations (8) are then closed by the integral condition

$$\int_0^\infty \left(\tilde{\boldsymbol{q}}^\dagger \cdot \frac{\partial \tilde{\boldsymbol{q}}}{\partial x}\right) \mathrm{d}y \Big/ \int_0^\infty \tilde{\boldsymbol{q}}^\dagger \cdot \tilde{\boldsymbol{q}} \, \mathrm{d}y = 0, \tag{10}$$

where † denotes the complex conjugate form. Equation (8) is then solved using a marching procedure where the wavenumber $\alpha$ is determined at each $x$-position using the iterative scheme

$$\alpha_{k+1} = \alpha_k + i \int_0^\infty \left(\tilde{\boldsymbol{q}}^\dagger \cdot \frac{\partial \tilde{\boldsymbol{q}}}{\partial x}\right) \mathrm{d}y \Big/ \int_0^\infty \tilde{\boldsymbol{q}}^\dagger \cdot \tilde{\boldsymbol{q}} \, \mathrm{d}y. \tag{11}$$

The imaginary part of $\alpha$ denotes the growth of the TS wave instability and is used to perform an $N$-factor calculation [17, 44] that is given by the expression

$$N = -\int_{x_0}^{x} \alpha_i(\zeta) \, \mathrm{d}\zeta. \tag{12}$$

For the subsequent stability analysis the maximum absolute value of the $u$-velocity perturbation field, $|u|_{\max}$, is used to draw direct comparisons between solutions of the PSE and LNS formulations.

The system of PSE equations (8) are solved subject to the no-slip conditions at the wall

$$u = v = T = 0 \quad \text{on} \quad y = 0, \tag{13a}$$

while the Dirichlet conditions are imposed in the freestream

$$u = v = T \to 0 \quad \text{as} \quad y \to \infty. \tag{13b}$$

The pressure $p$ is also assumed to satisfy the Dirichlet condition in the freestream.

Chordwise step-sizes $\Delta x$ were implemented, where the Li-Malik [37] stability restriction criteria $\Delta x > 1/|\alpha_r|$ was imposed to obtain numerically stable solutions. It should be noted that PSE analysis was also successfully undertaken for smaller $\Delta x$ than that imposed by the Li-Malik criterion. However, it was found that the best PSE-LNS comparisons arose for calculations based on $\Delta x$ that satisfied this criterion. As the size of the wavenumber $\alpha_r$ is dependant on the frequency of the TS wave, special care was required to ensure that the step-size limitation was satisfied for those PSE results presented. Additionally, to improve the numerical robustness of the method, the effect of the chordwise pressure gradient $\partial p/\partial x$ was suppressed.

### *2. LNS Scheme*

The LNS formulation for a compressible flow is presented within the appendices. In the far-field limit, Dirichlet conditions are imposed, where perturbations are assumed to have decayed to a negligible magnitude. On $y = 0$, the no-slip condition is generally enforced, where $u = v = T = 0$. Perturbations are then excited by a small periodic forcing, where the no-slip condition is defined as

$$u' = -h(x,t)U_{B,y}(x,0), \quad v' = \frac{\partial h(x,t)}{\partial t} \quad \text{and} \quad T' = -h(x,t)T_{B,y}(x,0) \quad \text{on} \quad y = 0, \tag{14a}$$

$$\Rightarrow u = -h(x)U_{B,y}(x,0), \quad v = -i\omega h(x) \quad \text{and} \quad T = -h(x)T_{B,y}(x,0) \quad \text{on} \quad y = 0, \tag{14b}$$

and the function $h(x)$ represents a normalised Gaussian distribution of the form

$$h(x) = 10^{-6}\exp\{-0.5([x - x_f]/\sigma)^2\}/\sqrt{2\pi\sigma^2}, \tag{15}$$

where $\sigma = 10$ and $x_f$ prescribe the variance and centre of the wall forcing, respectively.

The LNS system of equations were discretised and solved in the manner described by Mughal and Ashworth [30]. High order finite difference methods were implemented along the $x$-axis, while a pseudo-spectral approach was utilised in the wall normal $y$-direction. Along the $x$-direction, up to 8000 points were used over the chord domain considered and 81 points was deemed sufficient in $y$ to accurately resolve solutions. LNS solutions were then computed by decomposing the discretised formulation as a large lower-upper block factorisation matrix.

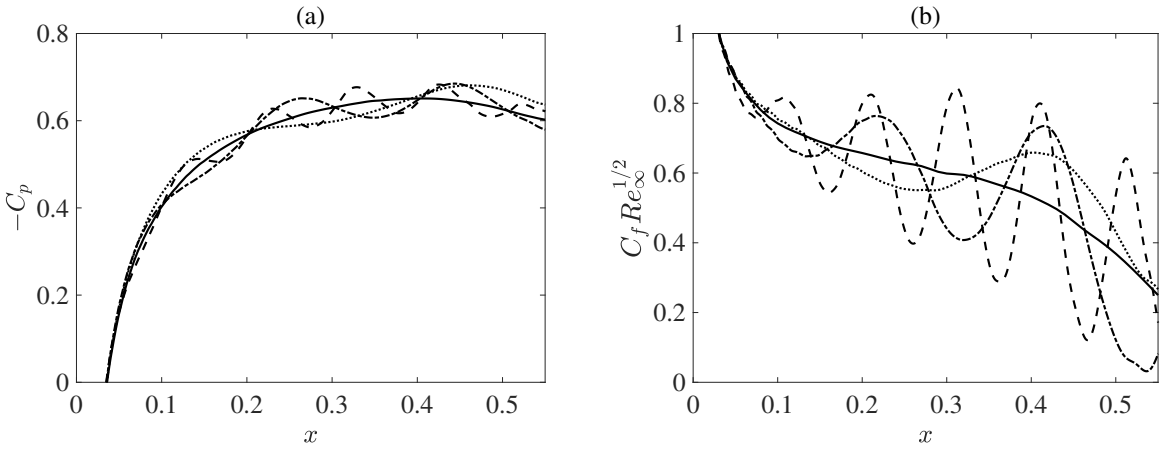


FIG. 3. Flow characteristics obtained using REBL for the surface configurations $\{\lambda, H\} = \{0, 0\}$ (solid line), $\{0.1, 0.0001\}$ (dashed), $\{0.2, 0.0002\}$ (chain) and $\{0.4, 0.0004\}$ (dotted). (a) Surface pressure coefficient $C_p$; (b) Skin friction coefficient $C_f Re_\infty^{1/2}$.

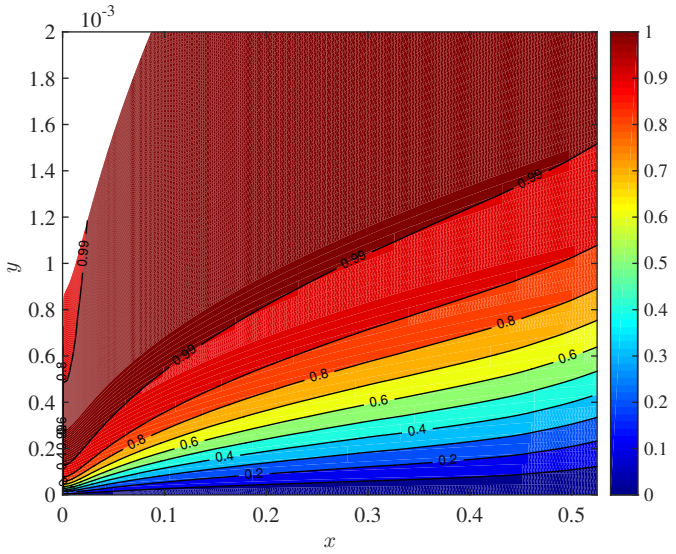


FIG. 4. Non-dimensional base flow $U_B$ obtained using REBL over a non-deformed wing in the $\{x, y\}$-plane.

## III. BASE FLOW

### A. Effect of Shallow Surface Waviness

Figure 3 illustrates the pressure $C_p$ and skin friction $C_f Re_\infty^{1/2}$ coefficients based on the boundary layer solutions generated by the REBL extraction method. Three wavy surface configurations are considered, where the freestream conditions are defined as $\{M_\infty, Re_\infty\} = \{0.7, 5 \times 10^6\}$ and the phase shift $\phi = 0$. Dashed lines depict solutions established over a surface with $\{\lambda, H\} = \{0.1, 0.0001\}$, while chain and dotted lines respectively represent the surface variations $\{\lambda, H\} = \{0.2, 0.0002\}$ and $\{0.4, 0.0004\}$. The solid lines display the results corresponding to that established on the non-deformed wing. Solutions are plotted against the $x$-direction and the effect of the sinusoidal wavy wall is shown to be mirrored in the two illustrated flow components. Furthermore, waviness can cause significant variations from the results obtained for the non-deformed wing. In particular the skin friction coefficient displays relatively large variations, with respective increases and decreases in $C_f Re_\infty^{1/2}$ corresponding to the flow passing over the crests and troughs of the wavy surface.

The non-dimensional $U_B$-velocity field for the non-deformed wing is plotted in figure 4 as a contour map in the

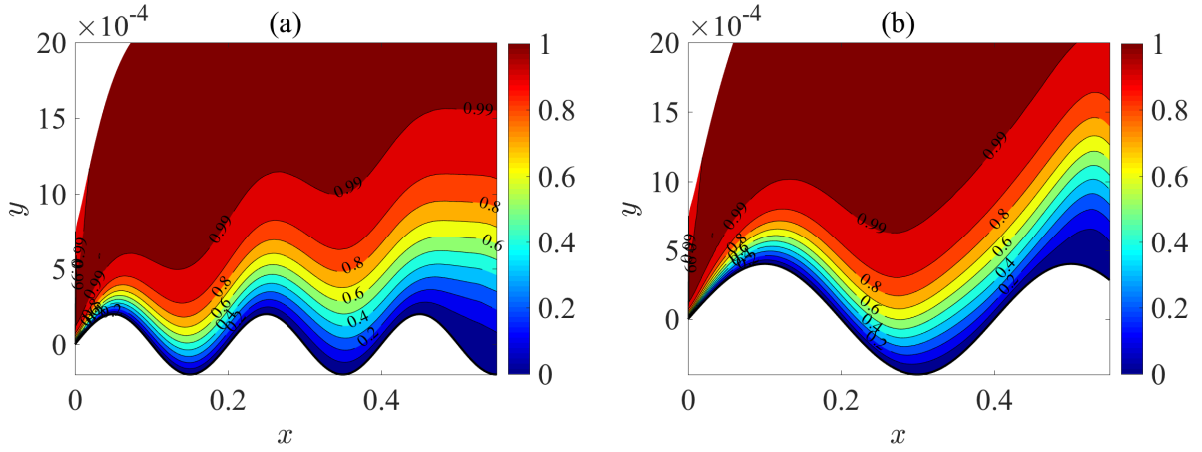


FIG. 5. Non-dimensional base flow $U_B$ obtained using REBL in the $\{x, y\}$-plane. (a) $\{\lambda, H\} = \{0.2, 0.0002\}$; (b) $\{0.4, 0.0004\}$.

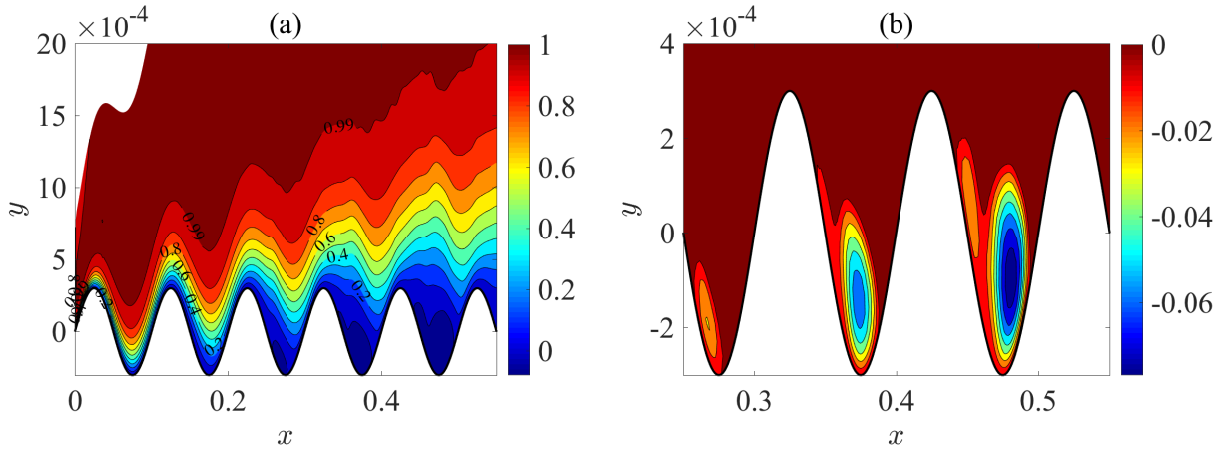


FIG. 6. (a) Illustration of the base flow $U_B$ obtained using REBL in the $\{x, y\}$-plane, over a wavy surface with $\{\lambda, H\} = \{0.1, 0.0003\}$. (b) Flow separation depicted within the troughs of the surface.

$\{x, y\}$-plane. Here we have used the coordinate scaling $\boldsymbol{x} = \boldsymbol{x}^*/c^*$ to present flow solutions, and since the chord length $c^* = 1$m, the coordinate axis can represent both dimensional and non-dimensional planes. Thus, the boundary layer is approximately 1mm thick. The undisturbed flow development over two wavy surfaces is depicted in figure 5, where the sinusoidal wall deformations are given as $\{\lambda, H\} = \{0.2, 0.0002\}$ and $\{0.4, 0.0004\}$, respectively. The $y$-axis has now been transformed to include the wavy surface variations, to help visualise behaviour of the flow as it passes over the crests and troughs of the surface. The reader is reminded that the vertical scale is very much smaller than that along the horizontal and if the flow was drawn using an equal axis the surface variation would be very difficult to distinguish. Nevertheless, the wavy wall has a relatively large impact on the flow development. In particular, the boundary layer thickness is found to vary significantly as the flow develops downstream, decreasing about the surface crests and increasing significantly near the troughs of the wavy wall. This behaviour is to be expected, as favourable and adverse pressure gradients are established about the respective crests and troughs of the surface.

### B. Separated Flows

Negative valued skin friction was not established for those wavy configurations drawn in figure 3(b). However, it was found that this eventually materialises for sufficiently large amplitudes $H$; finite regions of reversed flow form within the troughs of the wavy surface. Figure 6 depicts contours of the steady $U_B$-velocity field that develops over the wavy surface with $\{\lambda, H\} = \{0.1, 0.0003\}$. The non-dimensional velocity field is plotted for both an extensive spatial range in (a) and for a concentrated region that highlights flow reversal in (b). Stationary bounded regions of

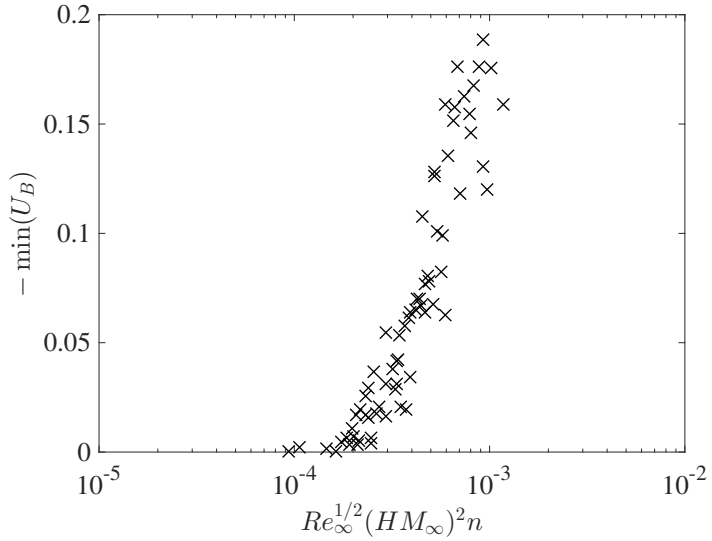


FIG. 7. Minimum value of the base flow $U_B$ against the function $Re_\infty^{1/2}(HM_\infty)^2 n$.

separation form within the troughs of the wavy surface, progressively increasing in magnitude and volume as the flow convects downstream. However, the maximum magnitude of the reverse flow depicted in figure 6 is less than 10% of the freestream amplitude, which is less than the suggested $15-30\%$ requirement to trigger absolute instability [35, 36]. Hence, we should only expect convective disturbances to develop over this particular wavy wing.

For $\lambda = 0.1$ and $\{M_\infty, Re_\infty\} = \{0.7, 5\times10^6\}$, amplitudes $H \geq 0.0002$ were sufficient to establish reverse flow, while for $\lambda \geq 0.2$, amplitudes $H > 0.0006$ were necessary. Greater precision in the value of $H$ needed to generate separation was not feasible, as we were only able to consider a finite number of surface deformations due to limited access to the TAU flow solver. Nevertheless, a crude relationship between the magnitude of the separation bubbles and the flow specifications can be deduced. Figure 7 displays the minimum value of the base flow $U_B$ that forms within the troughs of the wavy surface against the expression $Re_\infty^{1/2}(HM_\infty)^2 n$. A logarithmic-linear scaling has been utilised to map the computations, while $n$ denotes the number of waves between the attachment-line and the location that $U_B$ is a minimum. For instance, in figure 6 reverse flow is strongest about the centre of the troughs, located about $x = 0.275$, 0.375 and 0.475; hence, $n = 2.75$, 3.75 and 4.75, respectively. Given the logarithmic-linear relationship in figure 7 we find that reverse flow first appears for $Re_\infty^{1/2}(HM_\infty)^2 n$ of the order $10^{-4}$. As the subsequent study concerns only convectively growing TS disturbances, flow systems with $-\min(U_B) > 0.15$ were discounted from the following stability analysis, as there was a possibility that they could establish absolute instability [35, 36].

The skin friction coefficient and pressure gradient $P_{B,x} = P^*_{B,x}/(\rho^*_B U^{*2}_B)$ associated with the REBL generated flow illustrated in figure 6 are plotted in figure 8 using dashed curves, while the dotted curves represent the corresponding results computed using the CoBL boundary layer method. The form of the surface waviness is also included in figure 8(c) to help illustrate flow characteristics. Over the chord range $0 \leq x \leq 0.23$ the two sets of results are almost identical. However, the solution from the CoBL scheme ends abruptly about $x = 0.23$, which is indicated by a cross marker in figure 8(a, b). Boundary layer methods (that include CoBL) are based on a chordwise marching procedure [11, 33] that fail for particularly strong adverse pressure gradients. For the case considered here, CoBL breaks down when $P_{B,x} \approx 1.3$ and before the onset of boundary layer separation; the skin friction coefficient is positive about the chord location that CoBL exhibits non-convergence. Thus, separated flow is not necessarily required for the boundary layer method to fail. Nevertheless, using the REBL procedure (based on extracting the basic state directly from the TAU flow solutions), we are able to construct complete flow profiles up to the end of the chord domain considered. Relatively strong variations in both $C_f Re_\infty^{1/2}$ and $P_{B,x}$ are captured by the REBL procedure. The skin friction coefficient and pressure gradient respectively decrease and increase in size along the downward slopes of the surface waviness, while the opposite behaviour is found along the upward slopes. Strong adverse pressure gradients (positive $P_{B,x}$) form within the troughs of the surface and negative valued skin friction is found to develop about the three chord locations that correspond to regions of separated flow depicted in figure 6(b).

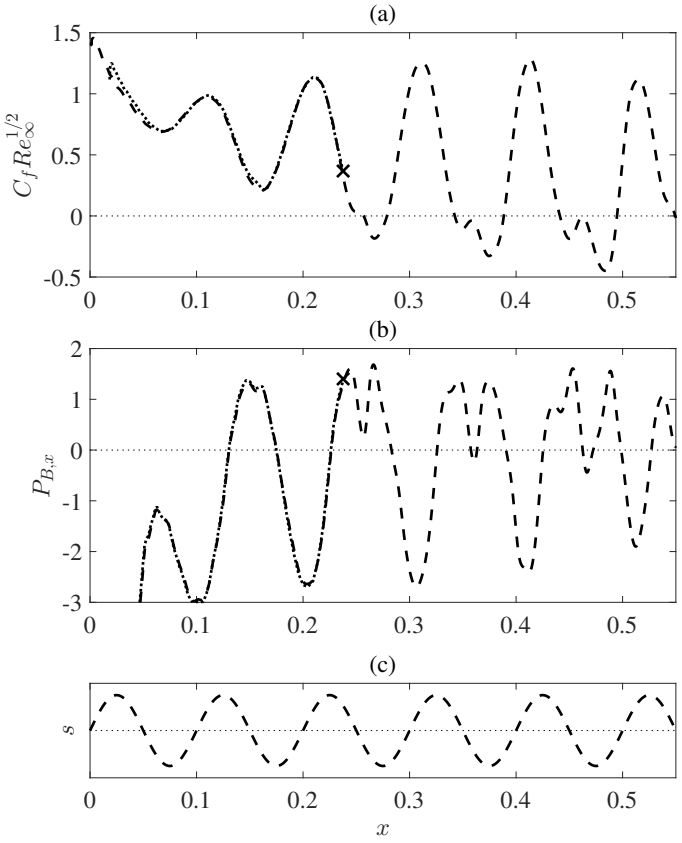


FIG. 8. Flow characteristics for the surface configuration $\{\lambda, H\} = \{0.1, 0.0003\}$ obtained using REBL (dashed) and CoBL (dotted). Cross-markers indicate the location that the CoBL method breaks down. (a) Skin friction coefficient $C_f Re_\infty^{1/2}$; (b) Pressure gradient $P_{B,x}$; (c) Surface variation $s$.

## IV. RESULTS

### A. REBL versus CoBL Stability Calculations

Stability analysis was undertaken for various surface configurations and non-dimensional frequencies $f \in [1 : 150] \times 10^{-6}$ (that corresponds to dimensional frequencies $f^* \in [1 : 30]$kHz). Unless stated otherwise, the freestream flow conditions were unchanged from that specified earlier; $\{M_\infty, Re_\infty\} = \{0.7, 5\times10^6\}$. Figure 9 compares the growth rates $\alpha_i$ and $N$-factor amplification rates of TS disturbances generated on three wavy surfaces for $f = 34 \times 10^{-6}$. The form of the surface waviness (4) has been included in the illustration to help draw conclusions, while the choice of frequency was made based on the strongest growing TS wave at $x \equiv x_{ref} = 0.55$ for the non-deformed wing (solid lines). Note that $x_{ref}$ represents a chord reference location that is used to compare stability calculations. For all three cases considered the flow remains attached at all chord locations $x \leq x_{ref}$. Thus, the PSE method can be utilised as there is no upstream propagation and we would only expect convective disturbances to develop [35, 36]. The dashed lines illustrate stability results based on the REBL generated boundary layers, while dotted lines depict the corresponding solutions for base flows established by CoBL. Results of the two sets of calculations are indistinguishable, at least up to the chord location (highlighted by a cross marker) that both methods were successfully able to compute solutions. However, at the cross markers, the CoBL method for generating the base flow breaks down, as the numerical model fails due to the appearance of a relatively large adverse pressure gradient (which is not necessarily sufficient to establish separation). Thus, downstream of the cross markers, PSE analysis could only be applied to the boundary layer solution established by REBL. For the remainder of this investigation we only consider linear stability of boundary layers generated by REBL.

Figure 9 also illustrates the strong influence of the surface waviness on the growth of the disturbance. Both $\alpha_i$ and

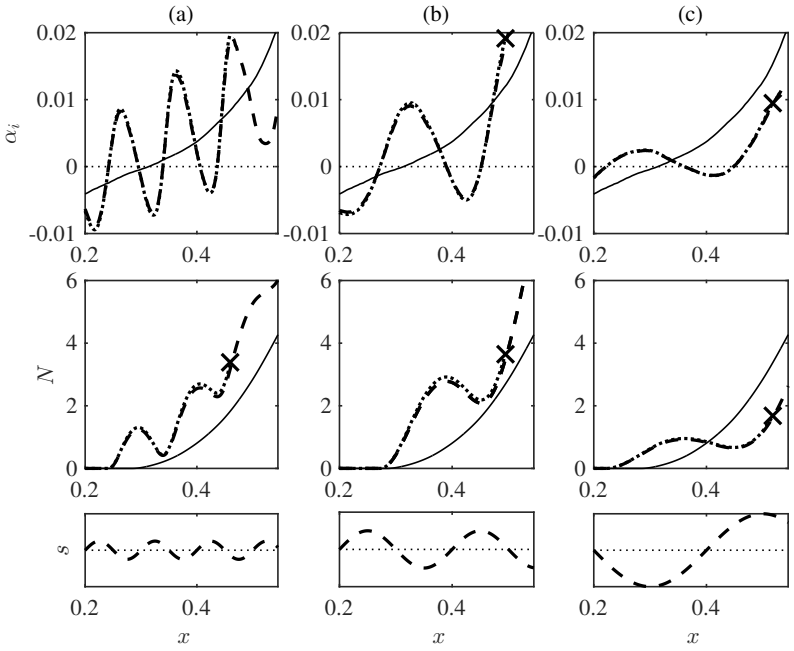


FIG. 9. Stability comparisons for base flows generated by REBL (dashed) and CoBL (dotted), for $f = 34 \times 10^{-6}$. Surface configurations are given as (a) $\{\lambda, H\} = \{0.1, 0.0001\}$; (b) $\{0.2, 0.0002\}$; (c) $\{0.4, 0.0004\}$. Cross-markers indicate the location that the CoBL method breaks down, and the solid curves represent the solutions associated with the non-deformed wing.

$N$ fluctuate in magnitude as the disturbance propagates downstream. The size of $\alpha_i$ increases along the downward slopes of the wavy surface, where strong adverse pressure gradients arise. Growth rates then attain local maxima about the troughs of the wave. Along the upward slopes of the wavy surface, favourable pressure gradients are generated that cause $\alpha_i$ to decrease. Local minimum growth rates are then found about the crests of the wave. The fluctuating growth rate then causes dips and rises in the $N$-factor, with the respective local maxima and minima located immediately downstream of the surface troughs and crests.

### B. LNS versus PSE Analysis for Separated Flow Systems

Figure 10 depicts the development of LNS generated $u$-velocity perturbation fields on five wavy wings. Tollmien-Schlichting disturbances were excited using a normalised Gaussian roughness centred about $x_f = 0.15$, for $f = 34 \times 10^{-6}$. The wavelength $\lambda = 0.1$ in all cases, while the amplitude $H$ increases in size from (a) through to (e). The wall-normal $y$-direction has again been deformed to include the sinusoidal surface variations, and the $u$-velocity fields have been normalised on their respective maximum absolute values $|u|_{\max}$ determined at each $x$-location. In the latter three subplots, regions of separation have been highlighted using solid black contours. For small $H$, disturbances display behaviour consistent with the expected TS wave evolution; the magnitude of the perturbation is largest within the boundary layer. However, as $H$ increases, the disturbance forms two equally strong peaks located about the surface troughs. This particular observation is best illustrated in figure 10(e) where the disturbance splits into two separate components as it emerges from the crests of the surface. The lower structure forms within the surface troughs, whilst the upper component develops directly above. As the disturbance approaches the end of each trough, the two parts of the TS wave re-coalesce. Similar behaviour was observed by Wie and Malik [20] on a wavy flat-plate, who stated that the disturbance was a mixed TS-Rayleigh type instability.

The maximum amplitude of the $u$-velocity field associated with disturbances plotted in figure 10 are illustrated in figure 11. Dashed lines represent the solutions established using the LNS formulation, while the dotted lines depict the corresponding PSE generated computations. Remarkably, the PSE and LNS results are (to the accuracy of the grid scale used) identical over the chord range shown for all wavy configurations considered. This result is quite surprising as the latter two flow systems contain rather large separation bubbles, and PSE methods are unable to resolve the effects of upstream propagating structures. This would suggest that the perturbations are primarily convective and that the regions of reverse flow do not engineer upstream disturbance development (at least not large enough to

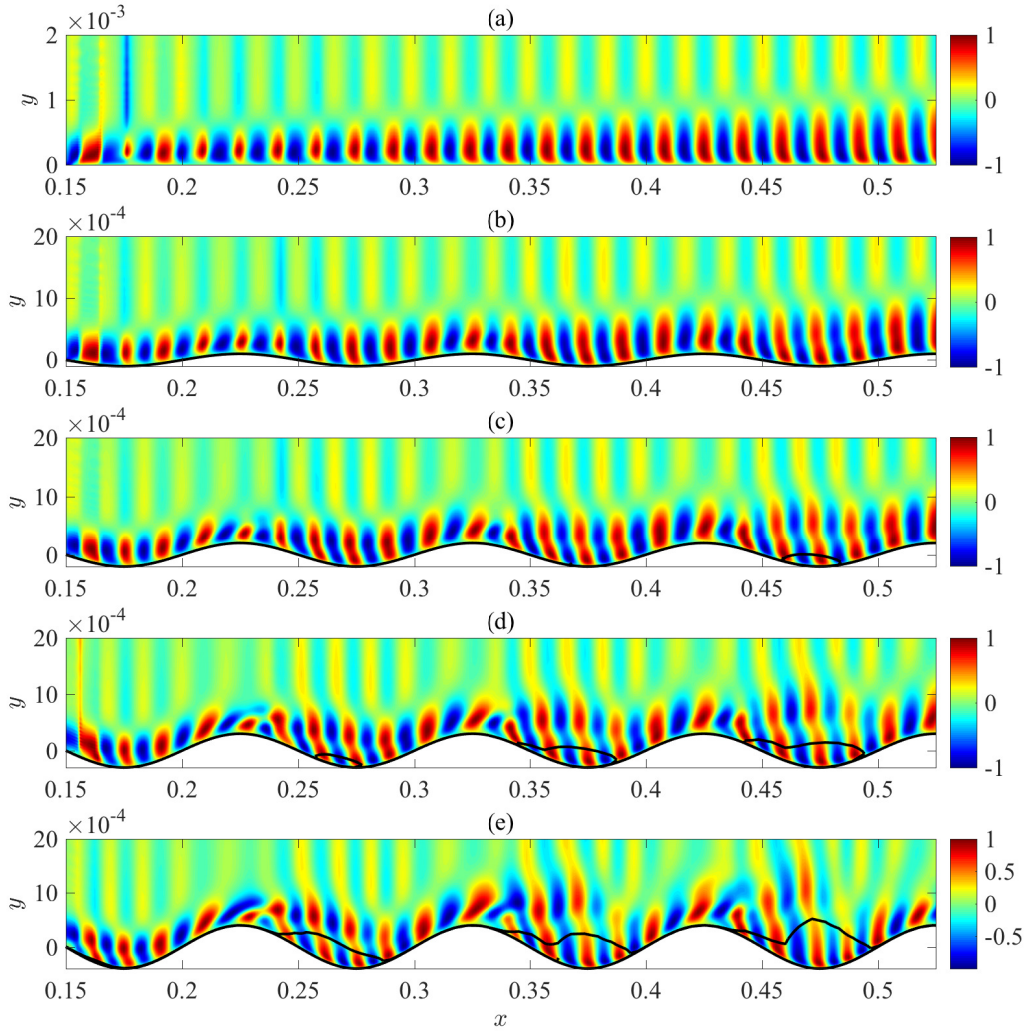


FIG. 10. Disturbance development $u/|u|_{\max}$, in the $\{x, y\}$-plane for $f = 34 \times 10^{-6}$ and $\lambda = 0.1$. (a) $H = 0.0$; (b) 0.0001; (c) 0.0002; (d) 0.0003; (e) 0.0004. Solid black curves highlight the local regions of separated flow.

establish significant variations between the PSE and LNS solutions). If upstream propagating perturbations and absolutely unstable behaviour were excited by the regions of separation, we might expect large differences between the two sets of calculations.

In order to achieve the excellent comparison between the two sets of solutions, the step size $\Delta x$ used to undertake the PSE analysis was carefully chosen to give the best comparison with that established via LNS. Initially we considered several step sizes and drew comparisons to determine the solution that gave the best accuracy. For the range of step sizes considered, the PSE method was able to successfully step through the separation bubbles, achieving numerically stable solutions for a range of $\Delta x$. PSE calculations were then scaled about $x = 0.3$ to match that established by the LNS model, and numerical differences between the two set of results were measured about $x = 0.5$ using the expression

$$\epsilon = \left| \frac{|u|_{\max,\mathrm{LNS}} - |u|_{\max,\mathrm{PSE}}}{|u|_{\max,\mathrm{LNS}}} \right| \times 100\%.$$

Differences $\epsilon$, for those disturbances considered in figures 10-11, are plotted in figure 12 against $|\alpha_r|\Delta x$. Numerically stable PSE calculations were obtained for smaller step-sizes than the Li-Malik critical value $|\alpha_r|\Delta x = 1$. However,

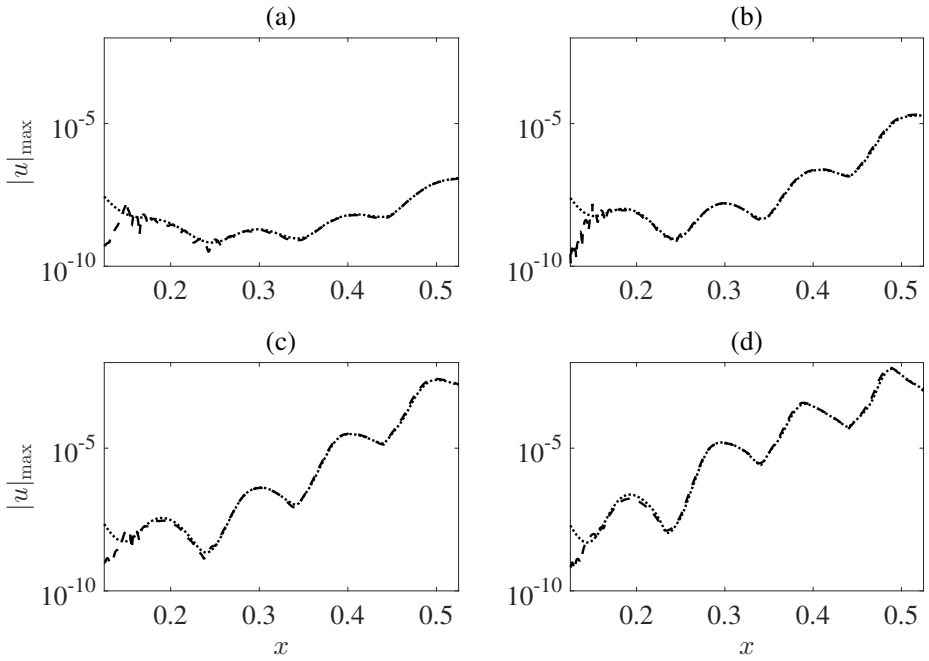


FIG. 11. Maximum absolute value of the $u$-velocity perturbation as a function of $x$ for $f = 34 \times 10^{-6}$ and $\lambda = 0.1$. Solutions generated for LNS (dashed lines) and PSE (dotted) methods. (a) $H = 0.0001$; (b) 0.0002; (c) 0.0003; (d) 0.0004.

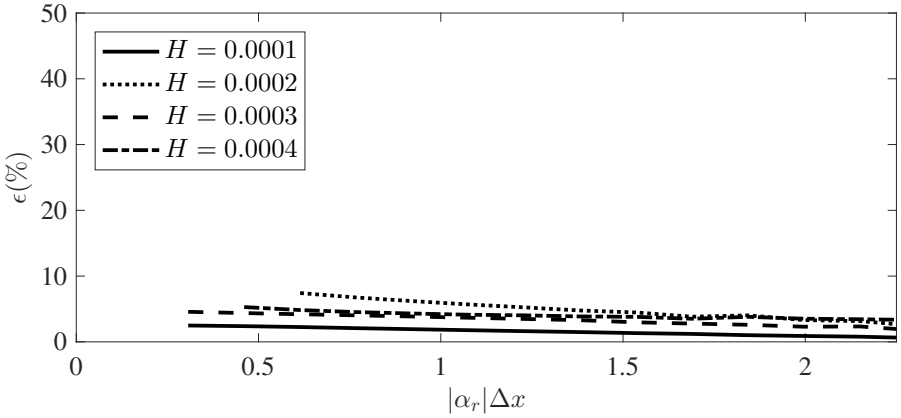


FIG. 12. Differences $\epsilon$ against the Li and Malik stability criterion $|\alpha_r|\Delta x$ for those disturbances considered in figures 10-11.

the smallest differences were obtained for $|\alpha_r|\Delta x > 1$. For the smallest amplitude, $H = 0.0001$, differences $\epsilon$ were less than 1%, while $\epsilon < 3\%$ was obtained for the largest amplitude, $H = 0.0004$. Some differences between the two sets of calculations should be expected, as the PSE method utilises approximations that neglect the higher order terms. Hence, for the frequency wave investigated above, the PSE formulation can be used to compute the magnitude of the disturbance to a reasonable degree of accuracy.

In addition to the above observations, figure 11 reveals several interesting disturbance characteristics. Firstly, the magnitude of the perturbations established for $H = 0.0003$ and 0.0004 are approximately the same near the end of the chord domain shown. Although this behaviour is initially surprising, we can attribute this particular observation to the large regions of separation that form within the troughs of the wavy surface; separation bubbles form a secondary wall that affects the evolution of the perturbation, establishing smaller amplification rates than that which might arise if separation did not occur. Secondly, it would appear that (at least for the frequency $f = 34 \times 10^{-6}$) regions of separated flow do not excite upstream propagating disturbances or absolutely unstable behaviour. This particular

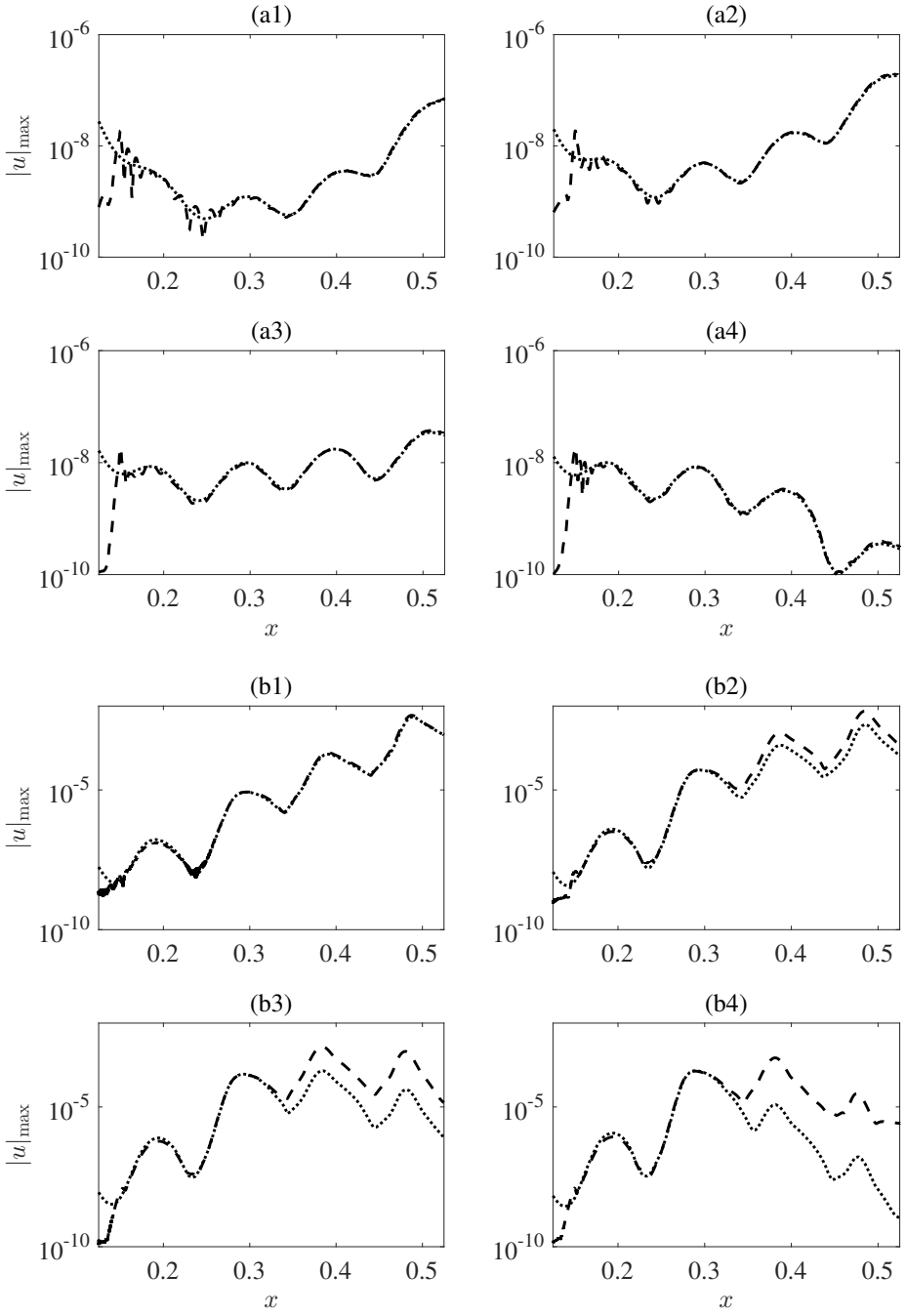


FIG. 13. Maximum absolute value of the $u$-velocity perturbation as a function of $x$. Solutions generated for (a) $\{\lambda, H\} = \{0.1, 0.0001\}$; (b) $\{0.1, 0.0004\}$; for LNS (dashed lines) and PSE methods (dotted). (1) $f = 31 \times 10^{-6}$; (2) $42 \times 10^{-6}$; (3) $52 \times 10^{-6}$; (4) $63 \times 10^{-6}$.

conclusion is drawn based on the fact that the PSE solutions are almost identical to that given by LNS, even though the former numerical scheme does not account for upstream propagating disturbances.

Further comparisons are drawn between the PSE and LNS solutions in figure 13. The magnitudes of four disturbances generated on wavy wings with the amplitudes $H = 0.0001$ and 0.0004 are depicted in figures 13(a) and 13(b), respectively. The line types are the same as that presented for figure 11, while the frequency $f \times 10^6 = 31, 42, 52$ and 63. Note that the step size implemented for the PSE analysis was based on that which satisfied the Li-Malik stability criterion and gave the smallest difference $\epsilon$. The LNS and PSE solutions are (to accuracy of the illustration) identical

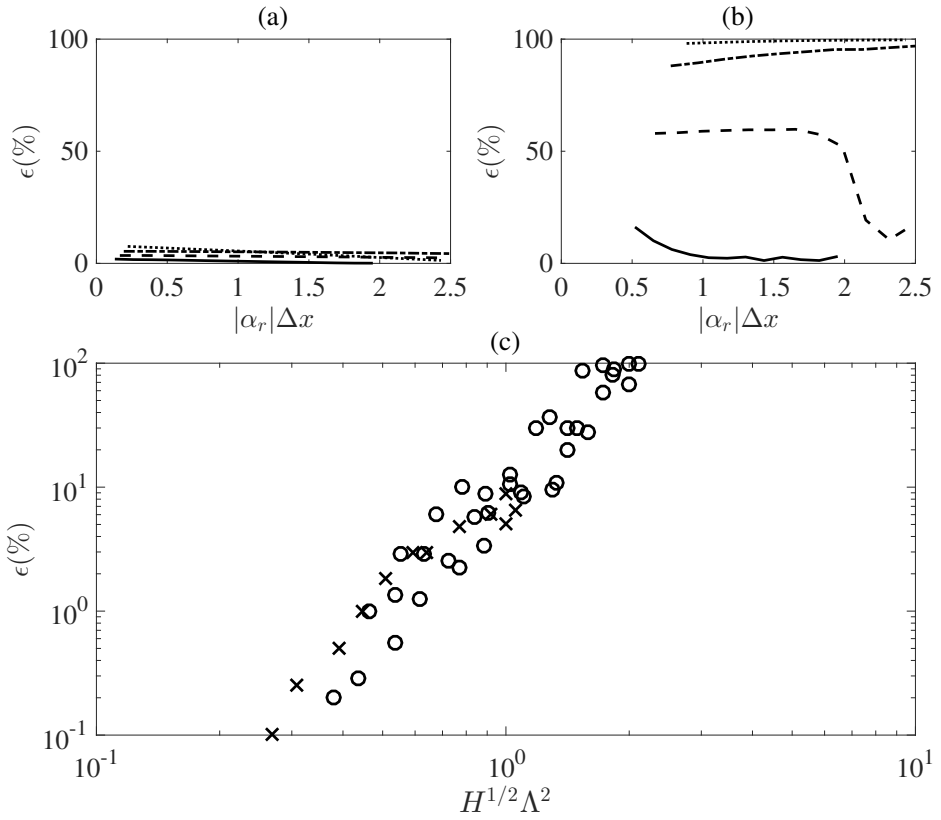


FIG. 14. (a, b) Differences $\epsilon$ against the Li and Malik stability criterion $|\alpha_r|\Delta x$ for $H = 0.0001$ and 0.0004. Frequencies $f = 31 \times 10^{-6}$ (solid line), $42 \times 10^{-6}$ (dashed), $52 \times 10^{-6}$ (chain) and $63 \times 10^{-6}$ (dotted). (c) Differences $\epsilon$ based on the optimum step-size conditions, as a function of $H^{1/2}\Lambda^2$ for $Re_\infty \times 10^{-6} = 2.5$, 5 and 7.5, and those frequencies considered in (a, b). $\Lambda = \lambda/\lambda_{\rm TS}$ is the number of TS waves per wavelength $\lambda$. Cross and circle markers respectively represent non- and separated flow systems.

for the $H = 0.0001$ configuration. The associated differences $\epsilon$ are plotted against $|\alpha_r|\Delta x$ in figure 14(a), and are less than 5% for all four frequencies.

For the larger surface variation $H = 0.0004$, the two sets of solutions are again in excellent agreement for the smallest of the frequencies considered ($f = 31 \times 10^{-6}$). However, as the TS frequency increases, the amplitudes of the PSE and LNS solutions diverge and the PSE method would appear to under-predict the growth of the disturbance. Furthermore, the magnitudes of $\epsilon$ associated with the larger frequencies (depicted in 14(b)) are found to approach 100%. Varying the step size $\Delta x$ was found to have little effect on the accuracy of the PSE calculations, with the method failing to establish converged solutions for step sizes outside of the limits considered in figure 14(b). Though not shown here, we included the effect of the higher-order PSE terms (often neglected in stability analysis [43]) and the chordwise pressure gradient that is usually suppressed; however their inclusion in the PSE analysis was not found to improve the accuracy of the computations.

The evolution of the four TS perturbations established for $H = 0.0004$ are depicted in figure 15. The vertical $y$-axis has again been deformed to include the surface variation and disturbances have been normalised using the local maximum amplitude. The structure of each perturbation is qualitatively similar to that described earlier; disturbances split into two equally strong components about the troughs of the surface and re-coalesce at the crests. Additionally, upstream propagating structures do not appear to be generated for any of the frequencies considered; disturbances develop only downstream and are convective. However, the wavelength $\lambda_{\rm TS}$ associated with each TS disturbance is clearly distinct and is found to decrease in size with increasing frequency. For $f = 31 \times 10^{-6}$, depicted in figure 15(a), the wavelength of the disturbance is approximately 1/50th of the chord length $c^*$ (or 2cm), with about five TS waves established per surface wavelength $\lambda = 0.1$. Meanwhile, for the larger frequency $f = 63 \times 10^{-6}$ (figure 15(d)), $\lambda_{\rm TS}$ is approximately 1cm and ten waves develop per wavelength $\lambda = 0.1$. Thus, larger $\epsilon$-differences coincide with a decreasing disturbance wavelength.

Given the above observations we attempt to determine a relationship between $\epsilon$, the surface configuration and the TS

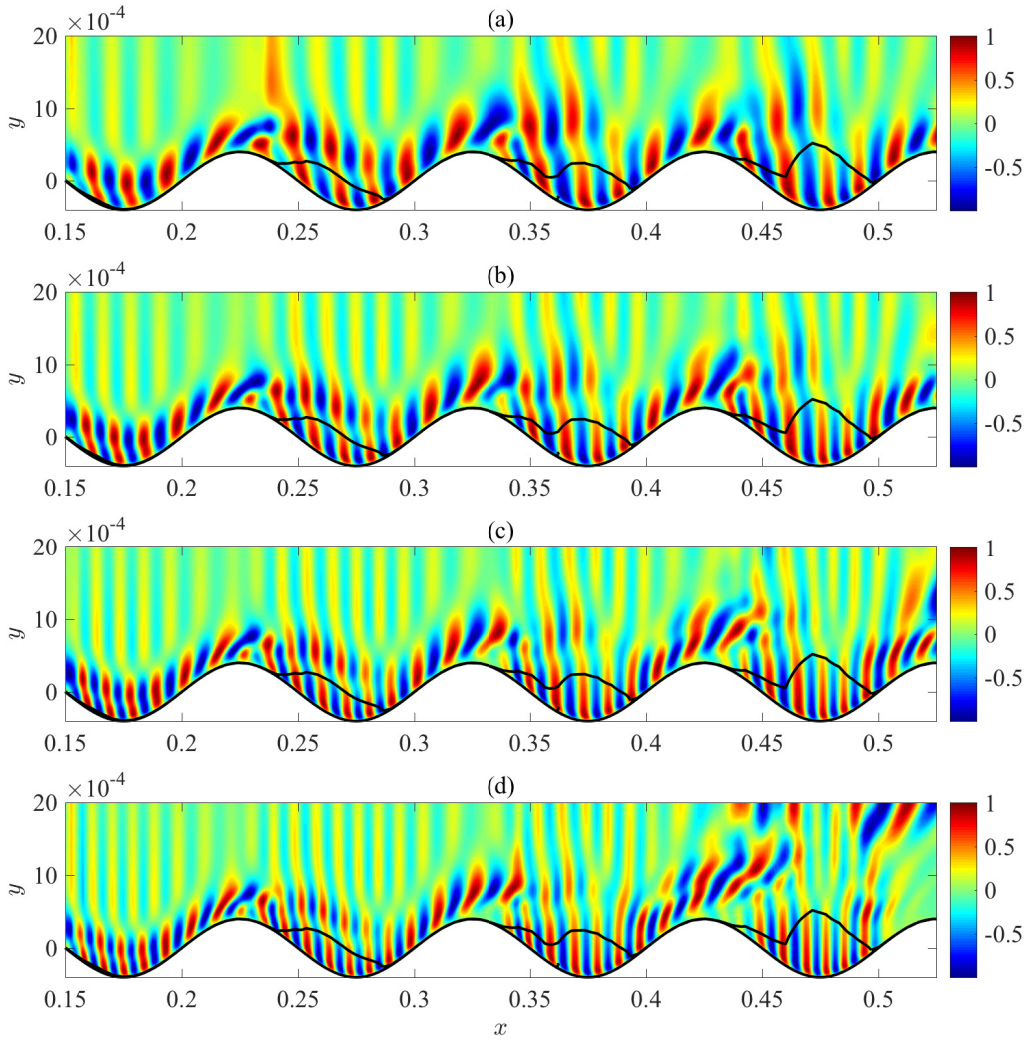


FIG. 15. Disturbance development $u/|u|_{\max}$, in the $\{x, y\}$-plane for $\{\lambda, H\} = \{0.1, 0.0004\}$. (a) $f = 31 \times 10^{-6}$; (b) $42 \times 10^{-6}$; (c) $52 \times 10^{-6}$; (d) $63 \times 10^{-6}$. Solid black curves highlight the local regions of separated flow.

wavelength. Differences $\epsilon$ are computed for all amplitudes $H \in [0 : 0.0001 : 0.0004]$, frequencies $f \times 10^6 = 31, 42, 52, 63$ and Reynolds numbers $Re_\infty \times 10^{-6} = 2.5, 5$ and 7.5. The step sizes $\Delta x$ used in the PSE calculations are again based on those solutions that give the best comparison with LNS. The resulting $\epsilon$-calculations are plotted against $H^{1/2}\Lambda^2$ in figure 14(c) using a log-log scaling. Cross and circle markers respectively represent non- and separated flow systems, while $\Lambda = \lambda/\lambda_{\rm TS}$ is the number of TS waves per wavelength $\lambda$. Surprisingly, $\epsilon$ is found to be approximately proportional (on the log-log scaling) to the function $H^{1/2}\Lambda^2$ and is independent of the Reynolds number. For small $H$ (non-separated flows) and sufficiently small $\Lambda$, $\epsilon < 10\%$. However, for separated flows (larger $H$) and large $\Lambda$, the $\epsilon$-differences increase greatly. Hence, our PSE-LNS analysis suggests that the accuracy of the PSE method is both dependant on the size of the surface variation (that establishes reverse flow), and the wavelength of the TS wave. If $\lambda_{\rm TS}$ is sufficiently large (about 2cm for the model considered herein), then PSE can be utilised to give very accurate solutions, including for those flow systems with large separation.

Reverse flow was not established for wavelengths $\lambda \geq 0.2$ and amplitudes $H \leq 0.0006$, which was the upper limit of our investigation. Nevertheless, we might expect that for parameter settings that establish separation, similar differences between the LNS and PSE calculations will be observed that are again dependant on the flow specifications and the wavelength of the TS wave instability.

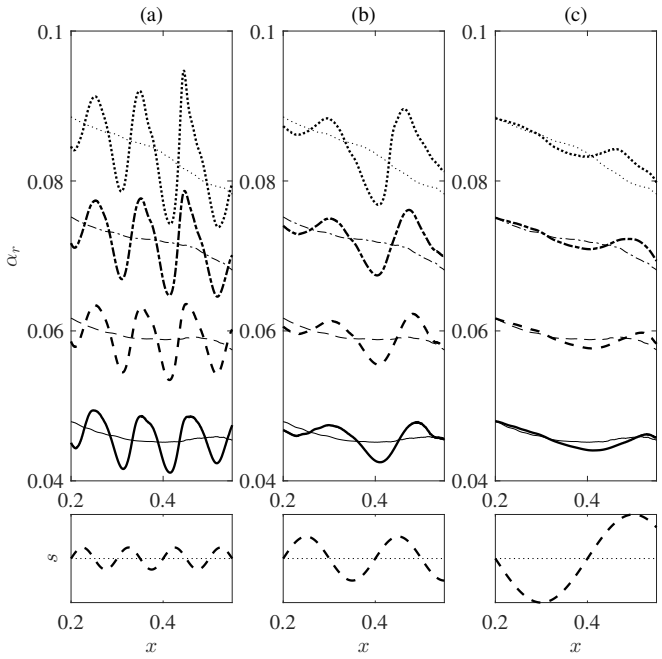


FIG. 16. The disturbance wavenumber $\alpha_r$ for frequencies $f = 31 \times 10^{-6}$ (solid thick line) $42 \times 10^{-6}$ (dashed) $52 \times 10^{-6}$ (chain) $63 \times 10^{-6}$ (dotted). (a) $\{\lambda, H\} = \{0.1, 0.0001\}$; (b) $\{0.2, 0.0002\}$; (c) $\{0.4, 0.0004\}$. Thinner line types depict the results established on the non-deformed wing.

### C. PSE Analysis for Non-Separated Flow Systems

For the remainder of this investigation, we only consider the development of disturbances in non-separated boundary layers; *i.e.* surface variations with a wavelength $\lambda \geq 0.2$ or $\{\lambda, H\} = \{0.1, 0.0001\}$. Additionally, the step-size $\Delta x$ used to undertake the following PSE analysis was carefully selected to satisfy the Li-Malik stability criterion.

#### *1. Variations in the Disturbance Wavenumber*

Figure 16 illustrates the evolutionary paths of the disturbance wavenumber $\alpha_r$ (thicker line types) that develops on three wavy surfaces. Calculations are given for four frequencies $f$, while the form of the surface waviness (4) has again been included to draw conclusions. The corresponding solutions on the non-deformed wing are drawn using thinner line types. Once again surface waviness establishes oscillatory behaviour in the disturbance characteristics, as the wavenumber increases and decreases as it develops downstream. Matching the oscillations in $\alpha_r$ with the form of the surface variation, $\alpha_r$ is found to grow towards a peak within the troughs of the surface wave and decreases to a local minimum about the crests. Furthermore, the surface waviness would appear to establish greater variations in $\alpha_r$ for larger frequencies. This particular observation is best illustrated in figure 16(a), by comparing the oscillatory variations found for $f = 31 \times 10^{-6}$ (solid curve) with that established for $f = 63 \times 10^{-6}$ (dotted). The latter result clearly depicts stronger fluctuations (compared to the non-deformed wing) that are spike-like in appearance. Additionally, as the wavelength $\lambda$ increases, the variations in $\alpha_r$ are significantly damped.

#### *2. Non-Parallel and Curvature Effects*

Non-parallel and surface curvature effects are examined in figure 17. Four wavy wall configurations are considered, where the frequency $f = 34 \times 10^{-6}$. Solid line types represent calculations based on the parallel flow approximation, while dashed and dotted lines respectively illustrate the non-parallel flow results without and with curvature effects. Surface curvature effects are included within the stability calculations by defining the parameters $\kappa$ and $\chi$ in (9) in terms of the wavy wing geometry. Similarly, they are removed from the two formulations by setting $\kappa = 0$ and $\chi = 1$.

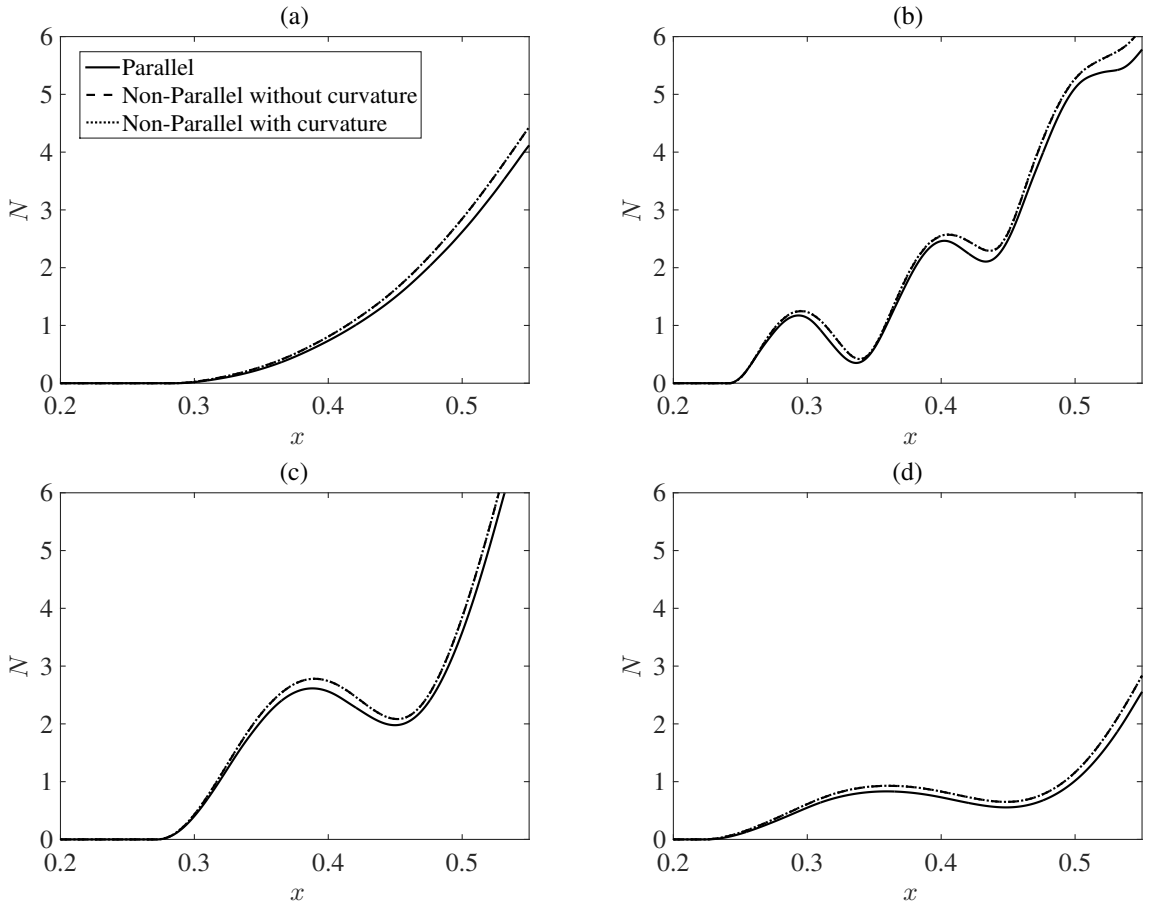


FIG. 17. Stability $N$-factor calculations for perturbations with frequency $f = 34 \times 10^{-6}$. Parallel flow results (solid line), non-parallel without curvature effects (dashed) and non-parallel with curvature effects (dotted). (a) $\{\lambda, H\} = \{0, 0\}$; (b) $\{0.1, 0.0001\}$; (c) $\{0.2, 0.0002\}$; (d) $\{0.4, 0.0004\}$.

Non-parallel flow effects are found to be very small, while curvature effects would appear to have no effect on the relative sizes of the $N$-factor.

### *3. Neutral Stability Curves*

Neutral stability curves are drawn in figure 18 in the $\{x, f\}$-plane for $\phi = 0$, where the unstable parameter space is enclosed by the curves. Three wavelengths $\lambda$ and varying amplitudes $H$ are considered, while results for the non-deformed wing are drawn using a solid curve. The illustrations highlight several interesting characteristics that are directly related to the form of the surface waviness. Firstly, the wavy walls establish a number of bounded regions of instability. Secondly, as the amplitude $H$ increases, the bounded regions of instability grow in size and unstable disturbances are obtained at larger frequencies. At a fixed frequency the flow develops downstream along the $x$-direction and passes through alternating stable and unstable sections of the stability parameter space. Thus, waviness forms finite regions of instability. In figure 18(a), surface waviness forms two bounded neutral stability curves that depict significantly different behaviour to the solution drawn for the non-deformed wing. However, as the wavelength increases, the effect of waviness would appear to diminish (as depicted in figure 18(c)); the solutions appear qualitatively similar to that established on the non-wavy wing. The chordwise oscillating pressure gradient that is engineered by the sinusoidal surface variation is the primary cause of these finitely bounded neutral stability curves. Waviness establishes both adverse and favourable pressure gradients that are sufficiently strong to destabilise and re-stabilise TS disturbances.

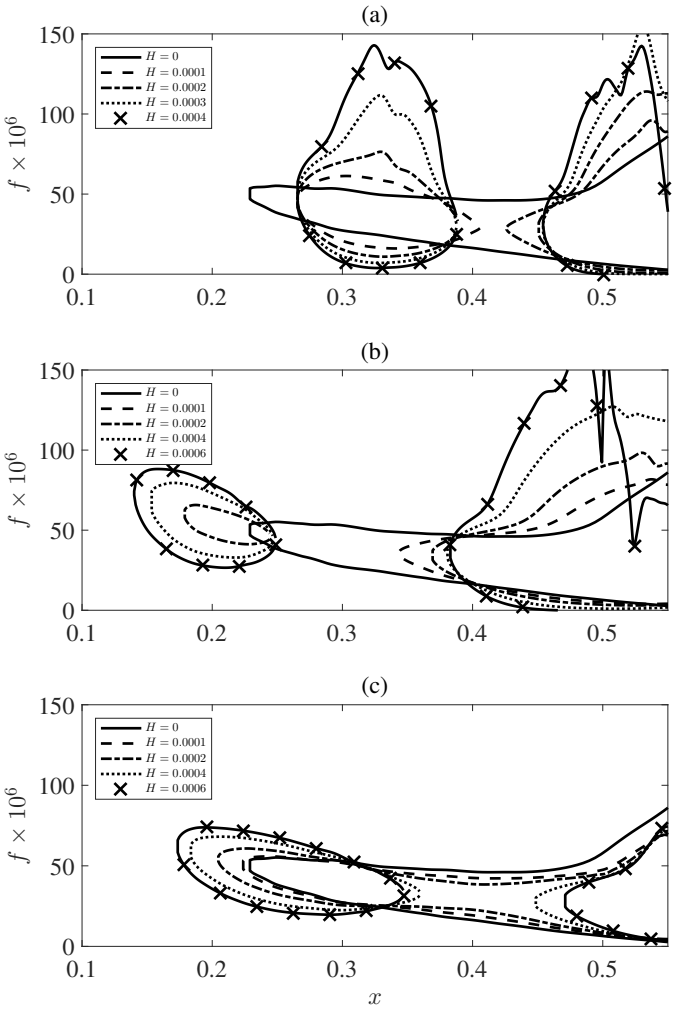


FIG. 18. Neutral stability curves for (a) $\lambda = 0.2$; (b) 0.3; (c) 0.4 and variable $H$.

### *4. Effect of Amplitude and Wavelength*

Figure 19 illustrates the effect of variable amplitude $H$ and wavelength $\lambda$ on the TS disturbance. The surface configurations considered in the three subplots are given as $\lambda \in [0.2 : 0.1 : 0.4]$, $H \in [0 : 0.0001 : 0.0006]$ and $\phi = 0$. The $N$-factor amplification rates are established by constructing envelopes of the strongest growing disturbances for all frequencies $f \in [1 : 150] \times 10^{-6}$. Effects of surface waviness are again mirrored in the stability calculations, as increases and decreases in the growth coincide with the respective regions of an adverse (near surface troughs) and favourable pressure gradient (crests). The onset of the TS wave instability can be forced to appear at a smaller $x$-position (as shown in figure 19(b) and $\lambda = 0.3$) or it can be delayed to locations downstream of that found on the non-wavy wing (as depicted in figure 19(a) and $\lambda = 0.2$). Furthermore, an unstable TS wave can be re-stabilised over some sections of the chord, before becoming unstable again further downstream. This particular observation is best illustrated in figure 19(b) about $0.3 < x < 0.4$.

Although waviness can suppress the initial onset of the TS wave instability, it is generally found that once the disturbance emerges, the amplification rate of the TS wave is enhanced. This is particularly true for $\lambda \leq 0.3$ and as the amplitude $H$ increases. For instance, the surface configuration $\{\lambda, H\} = \{0.2, 0.0003\}$ generates a disturbance (represented by a dotted line in figure 19(a)) with an amplification factor $N = 11$ at $x_{ref}$, while the non-wavy wing model establishes $N \approx 4.5$. Thus, waviness can considerably destabilise the TS disturbance. Furthermore, it was

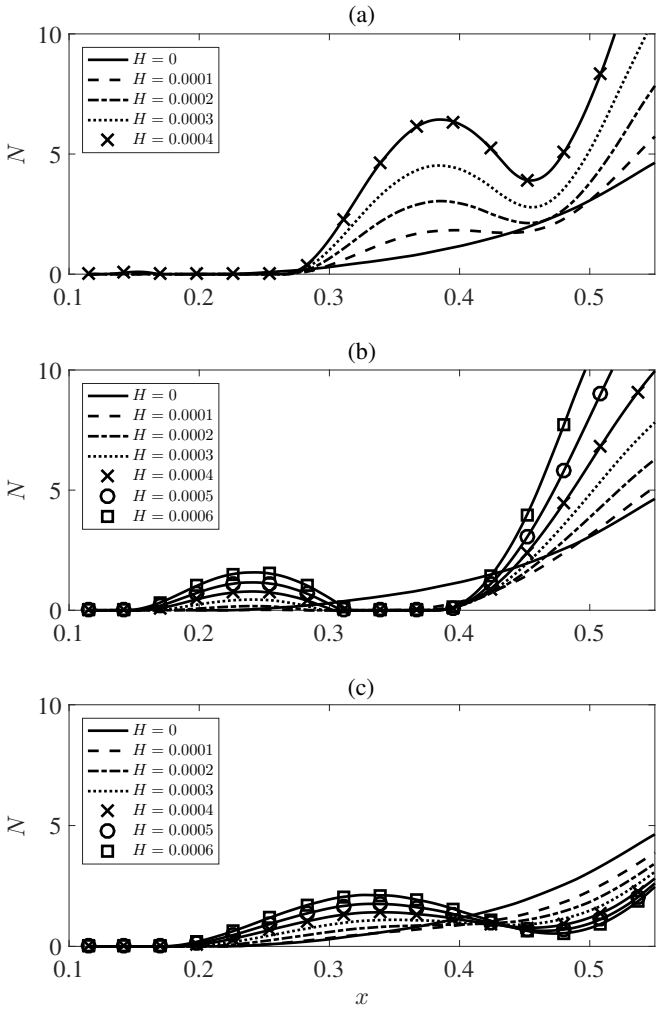


FIG. 19. Stability $N$-factor calculations for surface waviness configurations (a) $\lambda = 0.2$; (b) $\lambda = 0.3$; (c) $\lambda = 0.4$ and variable $H$.

determined that the $\Delta N$ variations at a fixed chord position are proportional to the square of the amplitude $H$, which is consistent with the conclusions of Wie and Malik [20]. Additionally, larger positive variations $\Delta N$ are found for smaller wavelengths $\lambda$. Hence, sinusoidal surface waviness generally increases the growth of the TS wave instability, which may in turn trigger the premature onset of transition to turbulence.

Stability calculations of the longer wavelength $\lambda = 0.4$ (plotted in figure 19(c)) are found to behave very differently to that given for the smaller wavelengths; this particular surface configuration significantly dampens the disturbance growth. About $x_{ref}$ the wavy surface $\{\lambda, H\} = \{0.4, 0.0006\}$ (that is represented by a solid line with square symbols) establishes $N \approx 2.5$, which is almost half of that given for the non-deformed wing. Hence, this particular surface variation is stabilising and may be a mechanism for delaying the onset of boundary layer transition. This observation was unanticipated as previous studies (Wie and Malik [20] amongst others) generally found that waviness destabilises the TS disturbances.

### *5. Effect of Phase*

The effect of a variable phase shift $\phi$ is considered in figure 20, where the $N$-factor envelopes are plotted for $\lambda \in [0.2 : 0.1 : 0.4]$ and $H = 0.0003$. From the three illustrations it is immediately obvious that the phase of the

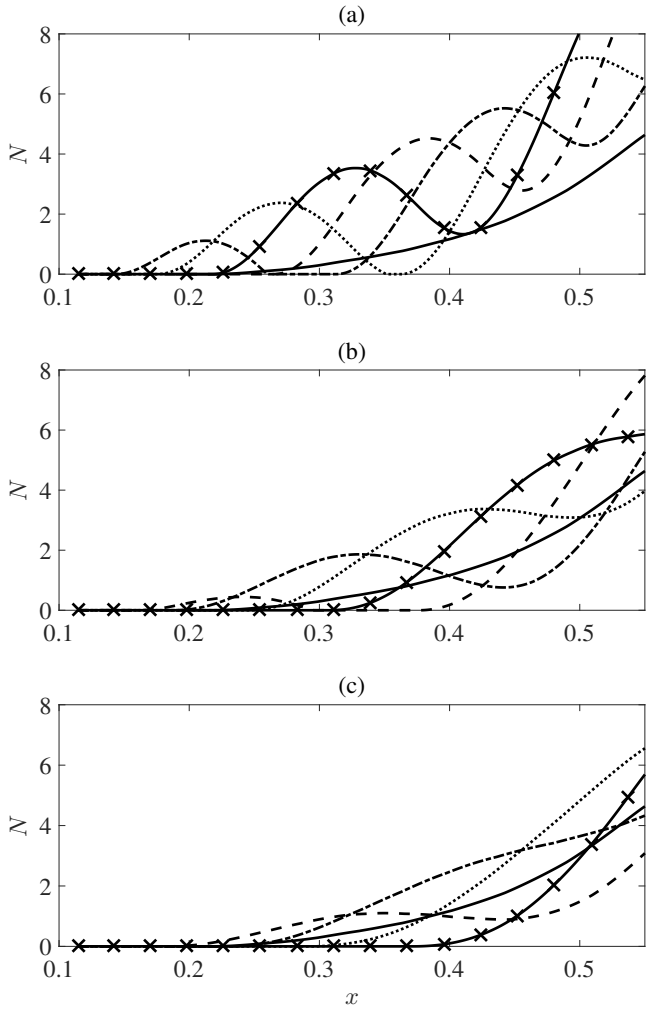


FIG. 20. Stability $N$-factor calculations for surface waviness configurations (a) $\{\lambda, H\} = \{0.2, 0.0003\}$; (b) $\{0.3, 0.0003\}$; (c) $\{0.4, 0.0003\}$, where the phase shift $\phi = 0$ (dashed), $\pi/2$ (chain), $\pi$ (dotted), $-\pi/2$ (solid with cross symbols). The solid line represents the solution on the non-deformed wing model.

surface waviness can have a significant impact on the evolution of the disturbance, as varying $\phi$ can cause the onset and size of the instability to vary greatly. For $\lambda = 0.2$ unstable behaviour is first excited for a phase shift $\phi = \pi/2$, while $\phi = 0$ generates the greatest delay in the onset of the instability. However, this does not necessarily imply that these surface configurations will respectively engineer the strongest or weakest growing disturbances. For instance, about $x_{ref}$, the TS wave generated on the wing with surface dimensions $\{\lambda, H, \phi\} = \{0.2, 0.0003, \pi/2\}$ (dotted line) has a smaller $N$-factor than that established for the other phase shifts considered, even though disturbances appear first for this particular configuration.

Figure 21 depicts the stability variations $\Delta N$ against the phase shift $\phi$. Computations are measured about the reference location $x_{ref}$ where the symbols illustrate the actual computations, with spline fitting used to plot a best-curve-fit. The phase of the surface waviness is found to establish significant variations in the TS wave growth rate. Although waviness generally establishes large positive $N$-factor variations, some configurations are stabilising; $\{\lambda, H, \phi\} = \{0.3, 0.0003, \pi\}$, $\{0.4, 0.0003, 0\}$ and $\{0.4, 0.0003, \pi/2\}$. Thus as suggested above, it may be possible to engineer a beneficial form of waviness that can be used to reduce instability and suppress the onset of transition.

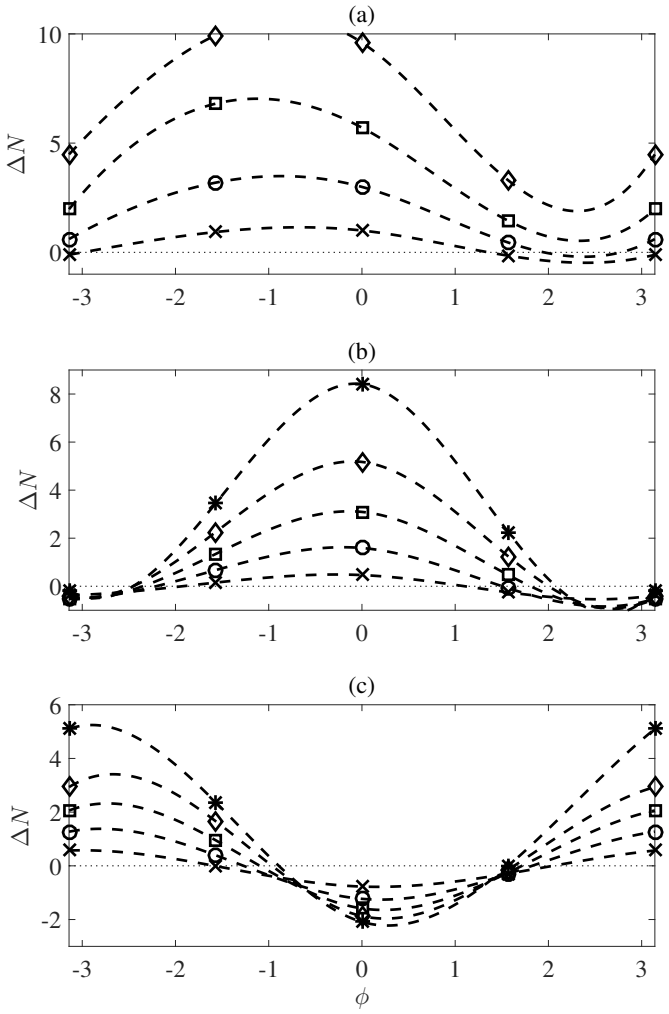


FIG. 21. Stability variations $\Delta N$ as a function of the phase shift $\phi$ measured about $x_{ref} = 0.55$. (a) $\lambda = 0.2$; (b) $\lambda = 0.3$; (c) $\lambda = 0.4$. The marker symbols $\times, \bigcirc, \square, \Diamond, *$ represent solutions of the respective amplitudes $H = 0.1, 0.2, 0.3, 0.4$ and 0.5. Dashed lines are spline fitted curves, linking the solutions of the same $H$.

### *6. Freestream Effects*

Table II tabulates the strongest growing frequencies and associated $N$-factor about $x_{ref}$ for variable $Re_\infty$ and $M_\infty$. In figure 22(a, c) $N$-factor envelopes are plotted for both the non-wavy wing model (thin line types) and surface dimensions $\{\lambda, H, \phi\} = \{0.2, 0.0002, 0\}$ (thick), where the flow conditions are as specified in the caption. The size of $N$ increases with the Reynolds number, for both the non-wavy and wavy surface. However, in figure 22(c) the strongest growing disturbance is found for $M_\infty = 0.25$ (dashed lines), with smaller $N$-factors found for lower and higher valued Mach numbers.

Stability variations $\Delta N$ are plotted against $Re_\infty$ and $M_\infty$ in figure 22(b, d). The $\Delta N$ computations are again based on the $N$-factor calculations established about $x_{ref}$. Cross symbols represent actual results with spline fitting used to draw a best-curve-fit. For wavelengths $\lambda \leq 0.3$ surface waviness is destabilising for all values of $Re_\infty$ and $M_\infty$ considered, while surfaces with a wavelength $\lambda = 0.4$ again engineer a decrease in the $N$-factor. In figure 22(b) the magnitude of $\Delta N$ is found to increase proportionally with $Re_\infty$, which is again consistent with the conclusions drawn by Wie and Malik [20]. Additionally, the absolute size of $\Delta N$ increases with the Mach number, particularly for $M_\infty > 0.5$.

| $Re_\infty \times 10^{-6}$ | $M_\infty$ | $f^*$(kHz) | $f \times 10^6$ | $N$ |
|---|---|---|---|---|
| 0.5 | 0.7 | 3 | 155 | 0.8 |
| 1 | 0.7 | 3.5 | 90 | 1.4 |
| 2.5 | 0.7 | 5 | 52 | 2.7 |
| 5 | 0.7 | 6.5 | 34 | 4.5 |
| 7.5 | 0.7 | 7 | 24 | 5.5 |
| 10 | 0.7 | 7 | 18 | 6.6 |
| 5 | 0.1 | 1 | 36 | 4.3 |
| 5 | 0.25 | 2.5 | 36 | 7.6 |
| 5 | 0.5 | 4.5 | 33 | 6.4 |

TABLE II. Strongest growing disturbance for variable freestream conditions about $x_{ref} = 0.55$ on the non-deformed wing.

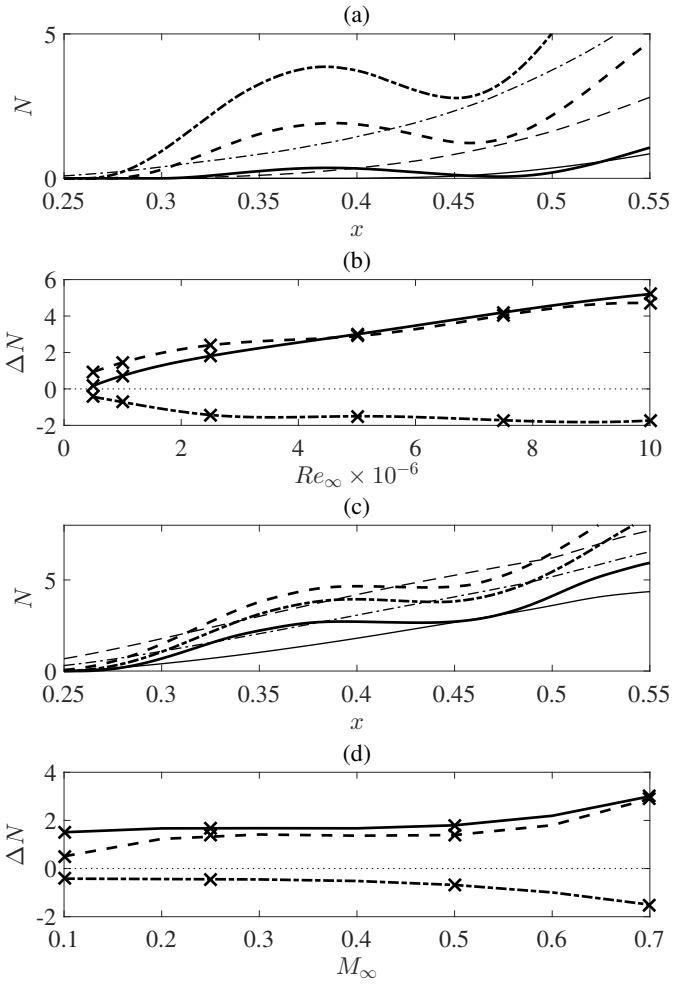


FIG. 22. (a) Stability $N$-factor calculations for $Re_\infty \times 10^{-6} = 0.5$ (solid lines), 2.5 (dashed) and 7.5 (chain) with $M_\infty = 0.7$. The fainter line types represent the solutions on the non-wavy surface and the thicker line types correspond to $\{\lambda, H, \phi\} = \{0.2, 0.0002, 0\}$. (b) Stability variation $\Delta N$ against $Re_\infty$ for $\{\lambda, H, \phi\} = \{0.2, 0.0002, 0\}$ (solid), $\{0.3, 0.0003, 0\}$ (dashed) and $\{0.4, 0.0004, 0\}$ (chain). (c) Stability $N$-factor calculations for $M_\infty = 0.1$ (solid lines), 0.25 (dashed) and 0.5 (chain) and $Re_\infty \times 10^{-6} = 5$. Line types are the same as (a). (d) Stability variation $\Delta N$ against $M_\infty$. Line types are the same as (b).

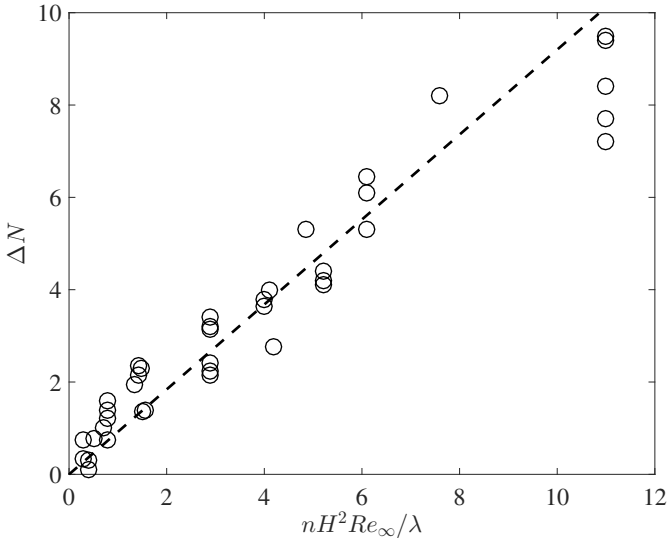


FIG. 23. Comparison between the variation $\Delta N$ (measured about $x_{ref}$) and $nH^2Re_\infty/\lambda$, for $f = 34\times10^{-6}$ ($f^* = 6.5$kHz) and $M_\infty = 0.7$.

### 7. *Comparison with Wie & Malik*

Given the above stability variations, we attempt to correlate results into an expression similar to that developed by Wie and Malik [20] for the flow over a wavy flat plate. The Wie and Malik expression (3) relates to a fixed freestream Mach number $M_\infty = 0.7$. Additionally, their analysis was applied to a fixed frequency that corresponded to the strongest growing disturbance on the non-deformed plate. Thus, to facilitate a comparable relationship, we only compare calculations established for $M_\infty = 0.7$ and $f = 34\times10^{-6}$ ($f^* = 6.5$kHz). Furthermore, due to the form of the waviness implemented in this study (imposed along the length of the wing with an origin located at the leading-edge), we must make some assumptions regarding how to collate comparable surface configurations and stability results.

PSE calculations for $f = 34\times10^{-6}$ measured about $x_{ref} = 0.55$, confirm that $\Delta N$ is proportional to both $Re_\infty$ and the square of the amplitude $H$ (or $h = 2H$ used in Wie and Malik). However, relating other surface characteristics (wavelength $\lambda$ and number of waves $n$ from the leading-edge) was more problematic. As surface waviness was implemented with a variable phase shift, the form of the wave at $x_{ref}$ could differ quite significantly. Thus, to successfully relate $\Delta N$ for variable surface dimensions it was necessary to compare only those wavy configurations with a comparable surface structure at $x_{ref}$. Circle symbols in figure 23 mark the stability variations $\Delta N$ against the function $nH^2Re_\infty/\lambda$ for those wavy surfaces with a trough centred near $x_{ref}$. For instance, the surface wave configuration $\{\lambda, H, \phi\} = \{0.2, H, 0\}$ forms a trough centred at $x_{ref}$, where the number of waves $n$ over the chord range $0 \le x \le x_{ref}$ is given as $n = 100x_{ref}/\lambda \equiv 2.75$. For those surface configurations that fall into this category, the corresponding values of $\Delta N$ are approximately located about the dashed line given as

$$\Delta N = 0.92nH^2Re_\infty/\lambda. \tag{16}$$

Thus, if a trough is centred about the reference location $x_{ref}$, the $\Delta N$ variations (for a fixed frequency) on the wavy wing are in reasonably good agreement with the analysis of Wie and Malik. However, after repeating the above procedure for surface configurations with a different wavy structure about $x_{ref}$, this particular relationship did not hold and the stability variations were scattered throughout the $(nH^2Re_\infty/\lambda, \Delta N)$-parameter space.

### 8. *First Disturbance to give $N = 4.5$*

Figure 24 depicts the chord location $x \equiv x_{N=4.5}$ against the corresponding disturbance frequency $f$ that first establishes an amplification factor $N = 4.5$. For instance, on the non-wavy wing, the strongest growing frequency $f = 34\times10^{-6}$ gives $N = 4.5$ at the reference location $x_{ref} \equiv x_{N=4.5}$. However, for wavy surfaces, the frequency responsible for the strongest growing TS wave was found to vary significantly. The corresponding results are marked

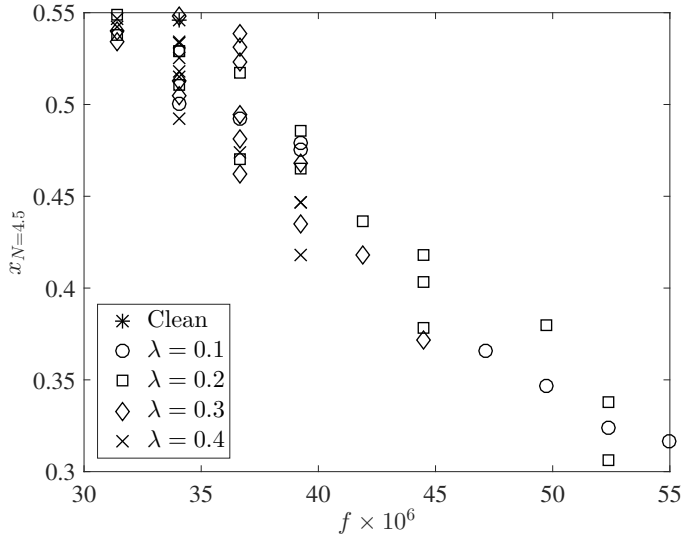


FIG. 24. The chord location $x_{N=4.5}$ plotted against the frequency $f$ that first establishes $N = 4.5$, for variable surface wave configurations. The freestream conditions $\{M_\infty, Re_\infty\} = \{0.7, 5 \times 10^6\}$.

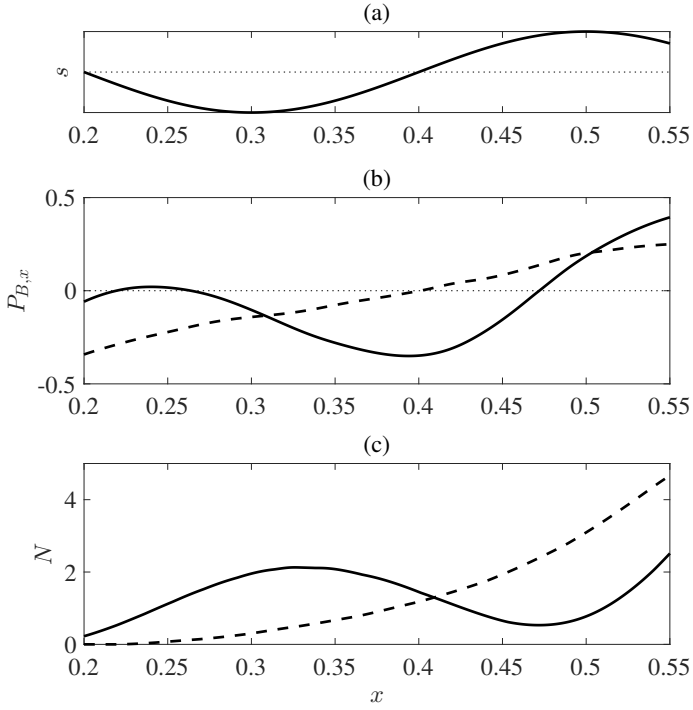


FIG. 25. Flow characteristics for the surface configuration $\{\lambda, H, \phi\} = \{0.4, 0.0006, 0\}$ (solid lines) and the non-deformed wing (dashed). (a) Form of the surface deformation $s$; (b) Pressure gradient $P_{B,x}$; (c) $N$-factor analysis.

in figure 23 for variable surface configurations and $\{Re_\infty, M_\infty\} = \{5 \times 10^6, 0.7\}$. The chord location $x_{N=4.5}$ is found to decrease with increasing $f$.

## V. CONCLUSIONS

The effect of long wavelength surface variations on an unswept infinite wing have been investigated. Compressible boundary layers were established using solutions of an industrial flow solver [28], while the stability and development of TS disturbances were studied using PSE and LNS methods. Wavy deformations were generally found to enhance the growth of the TS instability. This was especially true for smaller wavelength and larger amplitude surface variations. Varying the phase of the sinusoidal surface waviness was also found to engineer large differences in the TS disturbance development. Furthermore, the stability variations on some wavy surface configurations, measured about a fixed location and for a constant frequency, were found to behave in a manner consistent with the analysis and relationships formed by Wie and Malik [20] on a wavy flat plate. Thus, their simplified flat-plate model provides a very good prediction for the TS wave variations on a wavy wing.

Although waviness was generally found to destabilise TS disturbances, some longer wavelength deformations established a stabilising effect that may be used to delay the onset of transition beyond that specified on the non-deformed wing. Those surface variations that damped the growth of the TS wave were found to create a stronger favorable pressure gradient about sections of the wing that had previously been relatively weak or adverse. The stabilising effect is demonstrated in figure 25 that depicts the form of the surface variation $s$ and the associated pressure gradient $P_{B,x}$ and $N$-factor envelope that develop on the wavy wing $\{\lambda, H, \phi\} = \{0.4, 0.0006, 0\}$. Along the upward slopes of the wavy surface, $P_{B,x}$ is found to decrease in size and attains smaller values than that depicted on the non-deformed wing. The strong favourable pressure gradient then suppresses the growth of the disturbance and the $N$-factor is significantly reduced. Hence, this particular surface configuration establishes a smaller amplification rate over the chord range considered. The stabilising effect illustrated for this particular configuration (and some others) was quite surprising as waviness has previously been thought to only destabilise the TS wave instability. However, we should acknowledge that many of the earlier studies were concerned with the flow development on flat-plate geometries and that the application of surface waviness to an already curved wing body may explain why a stabilising effect can be achieved in some instances.

Boundary layers were extracted directly from the solutions of a full Navier-Stokes solver, allowing us to investigate the evolution of disturbances in separated boundary layers. The extent of the separation bubbles that could form within the troughs of the wavy surface was found to increase with the amplitude $H$; for surface wavelengths $\lambda = 0.1$, $H \geq 0.002$ was sufficient to establish separated flow. Although the PSE model does not account for the upstream propagation associated with reverse flow, we were still able to successfully apply the PSE method in most cases. Furthermore, for flows with small separation bubbles, PSE calculations were shown to be in excellent agreement with the LNS computations provided the wavelength of the TS disturbance was sufficiently long. Differences between the PSE and LNS modelling were shown to be proportional to $H^{1/2}\Lambda^2$ on a log-log mapping, where $\Lambda$ is the ratio of the surface wavelength $\lambda$ to the TS wavelength $\lambda_{\mathrm{TS}}$. Thus, the accuracy of the PSE model was found to be dependant on the wavelength of the TS wave; if $\Lambda$ is relatively small, then the PSE method could accurately compute the disturbance development in separated boundary layers. However, for $\Lambda \gtrsim 5$ (shorter TS wavelengths $\lambda_{\mathrm{TS}}$), the PSE method was found to greatly under predict the amplification rate of the TS disturbance.

## ACKNOWLEDGMENTS

This work has been supported by the EPSRC funded LFC-UK project: Development of Under-Pinning Technology for Laminar Flow Control, grant EP/I037946/1 and by the TSB funded ALFET project 113022. We thank the referees for many helpful suggestions concerning the presentation and improvement of our results.

### Appendix A: LNS Formulation

The LNS continuity, momentum and energy equations in a 2D compressible flow are given as

$$\chi u_x + \frac{\chi\rho_{B,x}}{\rho_B}u + \left\{\frac{\rho_{B,y}}{\rho_B} - \kappa\chi\right\}v + v_y + \frac{\chi U_B p_x + V_B p_y}{P_B} - \frac{(\chi U_B T_x + V_B T_y)}{T_B} - \left\{i\omega - \chi(U_{B,x} - \kappa V_B) - V_{B,y} + \frac{(\chi U_B T_{B,x} + V_B T_{B,y})}{T_B}\right\}\frac{p}{P_B} + \left\{i\omega - \chi(U_{B,x} - \kappa V_B) - V_{B,y} - \frac{\chi U_B \rho_{B,x} + V_B \rho_{B,y}}{\rho_B} + \frac{(\chi U_B T_{B,x} + V_B T_{B,y})}{T_B}\right\}\frac{T}{T_B} = 0, \quad \text{(A1a)}$$

$$\frac{u_{yy}+r\chi^2u_{xx}}{Re}+\frac{s\chi v_{xy}}{Re}+\frac{\rho_B}{\mu_B P_B}\Big\{\chi U_B(\kappa V_B-U_{B,x})-V_BU_{B,y}\Big\}p-\frac{\chi}{\mu_B}p_x-\Big\{\frac{\rho_B}{\mu_B}\Big(\chi(U_{B,x}-\kappa V_B)-i\omega\Big)+\frac{\kappa^2\chi^2}{Re}-\frac{\kappa\chi\mu_{B,y}}{\mu_BRe}\Big\}u-\Big\{\frac{\rho_BV_B}{\mu_B}+\frac{\kappa\chi}{Re}-\frac{\mu_{B,y}}{\mu_BRe}\Big\}u_y+\Big\{\frac{\rho_B}{\mu_B}\Big(\kappa\chi U_B-U_{B,y}\Big)-\frac{r\kappa\chi^2\mu_{B,x}}{\mu_BRe}\Big\}v+\frac{m\chi\mu_{B,x}}{\mu_BRe}v_y-\Big\{\frac{\rho_BU_B}{\mu_B}-\frac{r\chi\mu_{B,x}}{\mu_BRe}\Big\}\chi u_x-\Big\{\frac{e\kappa\chi}{Re}-\frac{\mu_{B,y}}{\mu_BRe}\Big\}\chi v_x+\frac{f_T}{\mu_BRe}\Big\{\Big(mV_{B,y}+r(\chi U_{B,x}-\kappa\chi V_B)\Big)\chi T_x+\Big(U_{B,y}+\chi(V_{B,x}+\kappa U_B)\Big)T_y\Big\}+\Big\{\frac{f_{TT}}{\mu_BRe}\Big(\chi T_{B,x}(r\chi[U_{B,x}-\kappa V_B]+mV_{B,y})+T_{B,y}(\chi[\kappa U_B+V_{B,x}]+U_{B,y})\Big)-\frac{\rho_B}{\mu_BT_B}\Big(\kappa\chi U_BV_B-\chi U_BU_{B,x}-V_BU_{B,y}\Big)+\frac{f_T}{\mu_BRe}\Big(U_{B,yy}-\kappa\chi(\kappa\chi U_B+U_{B,y})-e\kappa\chi^2V_{B,x}+s\chi V_{B,xy}+r\chi^2U_{B,xx}\Big)\Big\}T=0, \tag{A1b}$$

$$\frac{rv_{yy}+\chi^2v_{xx}}{Re}+\frac{s\chi u_{xy}}{Re}-\frac{\rho_B}{\mu_BP_B}\Big\{\chi U_B(\kappa U_B+V_{B,x})+V_BV_{B,y}\Big\}p-\frac{p_y}{\mu_B}-\Big\{\frac{\rho_B}{\mu_B}\Big(V_{B,y}-i\omega\Big)+\frac{r\kappa^2\chi^2}{Re}+\frac{m\kappa\chi\mu_{B,y}}{\mu_BRe}\Big\}v-\Big\{\frac{\rho_BV_B}{\mu_B}+\frac{r\kappa\chi}{Re}-\frac{r\mu_{B,y}}{\mu_BRe}\Big\}v_y-\Big\{\frac{\rho_B}{\mu_B}\Big(2\kappa\chi U_B+\chi V_{B,x}\Big)-\frac{\kappa\chi^2\mu_{B,x}}{\mu_BRe}\Big\}u+\frac{\chi\mu_{B,x}}{\mu_BRe}u_y-\Big\{\frac{\rho_BU_B}{\mu_B}-\frac{\chi\mu_{B,x}}{\mu_BRe}\Big\}\chi v_x+\Big\{\frac{e\kappa\chi}{Re}+\frac{m\mu_{B,y}}{\mu_BRe}\Big\}\chi u_x+\frac{f_T}{\mu_BRe}\Big\{\Big(rV_{B,y}+m\chi(U_{B,x}-\kappa V_B)\Big)T_y+\Big(\chi(\kappa U_B+V_{B,x})+U_{B,y}\Big)\chi T_x\Big\}+\Big\{\frac{f_{TT}}{\mu_BRe}\Big(T_{B,y}(m\chi[U_{B,x}-\kappa V_B]+rV_{B,y})+\chi T_{B,x}(\chi[\kappa U_B+V_{B,x}]+U_{B,y})\Big)+\frac{\rho_B}{\mu_BT_B}\Big(\chi U_B(\kappa U_B+V_{B,x})+V_BV_{B,y}\Big)+\frac{f_T}{\mu_BRe}\Big(r(V_{B,yy}-\kappa\chi[\kappa\chi V_B+V_{B,y}])+e\kappa\chi^2U_{B,x}+s\chi U_{B,xy}+\chi^2V_{B,xx}\Big)\Big\}T=0, \tag{A1c}$$

$$\frac{T_{yy}+\chi^2T_{xx}}{Re}+\frac{\Gamma}{\mu_B}\Big\{\chi U_Bp_x+V_Bp_y\Big\}-\Big\{\frac{i\omega\Gamma}{\mu_B}+\frac{\sigma\rho_B}{\mu_BP_B}\Big(\chi U_BT_{B,x}+V_BT_{B,y}\Big)\Big\}p+\Big\{\frac{\chi(f_TT_{B,x}+\mu_{B,x})}{\mu_BRe}-\frac{\sigma\rho_BU_B}{\mu_B}\Big\}\chi T_x+\Big\{\frac{f_TT_{B,y}+\mu_{B,y}}{\mu_BRe}-\frac{\sigma\rho_BV_B}{\mu_B}-\frac{\kappa\chi}{Re}\Big\}T_y+\Big\{\frac{\chi(\Gamma P_{B,x}-\sigma\rho_BT_{B,x})}{\mu_B}+\frac{2\Gamma}{Re}\Big(\kappa\chi(\chi[\kappa U_B+V_{B,x}]+U_{B,y})\Big)\Big\}u+\Big\{\frac{\Gamma P_{B,y}-\sigma\rho_BT_{B,y}}{\mu_B}+\frac{2\Gamma}{Re}\Big(\kappa\chi(r\chi[\kappa V_B-U_{B,x}]-mV_{B,y})\Big)\Big\}v+\frac{2\Gamma}{Re}\Big\{\chi(\kappa U_B+V_{B,x})+U_{B,y}\Big\}u_y+\frac{2\Gamma}{Re}\Big\{m\chi(U_{B,x}-\kappa V_B)+rV_{B,y}\Big\}v_y+\frac{2\Gamma}{Re}\Big\{r\chi(U_{B,x}-\kappa V_B)+mV_{B,y}\Big\}\chi u_x+\frac{2\Gamma}{Re}\Big\{\chi(\kappa U_B+V_{B,x})+U_{B,y}\Big\}\chi v_x+\Big\{\frac{\sigma\rho_B}{\mu_B}\Big(\frac{\chi U_BT_{B,x}+V_BT_{B,y}}{T_B}+i\omega\Big)+\frac{f_{TT}}{\mu_BRe}\Big(T_{B,y}^2+\chi^2T_{B,x}^2\Big)+\Big(\chi^2T_{B,xx}+T_{B,yy}-\kappa\chi T_{B,y}+\Gamma\Big(\kappa^2\chi^2U_B^2+rV_{B,y}^2+r\chi^2(U_{B,x}-\kappa V_B)^2+2m\chi V_{B,y}(U_{B,x}-\kappa V_B)+2\kappa\chi U_B(U_{B,y}+\chi V_{B,x})+(U_{B,y}+\chi V_{B,x})^2\Big)\Big)\frac{f_T}{\mu_BRe}\Big\}T=0, \tag{A1d}$$

where $Re$ is the Reynolds number based on the boundary layer thickness $\delta^*$. Subscripts $x$ and $y$ denote the derivatives along the respective chordwise and wall-normal directions. The parameters $\Gamma=(\gamma-1)M_\infty^2\sigma$, $e=r+1$, $r=s+1$, $s=m+1$ and $m=-2/3$. Here $\mu_B=f(T)$ is the dependence of the dynamic viscosity on the temperature and

$f_T = d\mu_B/dT$, $f_{TT} = d^2\mu_B/dT^2$. Further, $\sigma$ represents the Prandtl number and $\gamma$ is the ratio of the specific heats.

---


[1] R. Ashworth and S. M. Mughal, "Modeling three dimensional effects on cross flow instability from leading edge dimples," in *IUTAM ABCM Symposium on Laminar Turbulent Transition* (2015) pp. 201–210.

[2] A. Fage, "The smallest size of spanwise surface corrugation which affects boundary-layer transition on an airfoil," (1943), Aeronautical Research Council, R & M 2120.

[3] B. H. Carmichael, R. C. Whites, and W. Pfenninger, "Low drag boundary layer suction experiments in flight on the wing glove of an f-94a airplane," (1957), Northrop Corp. Report No. NAI-57-1163 (BLC-101).

[4] B. H. Carmichael, "Surface waviness criteria for swept and unswept laminar suction wings," (1959), Northrop Corp., Report No. NOR-59-438 (BLC-123).

[5] B. H. Carmichael and W. Pfenninger, "Surface imperfection experiments on a swept laminar suction wing," (1959), Northrop Corp., Report No. NOR-59-454 (BLC-124).

[6] B. J. Holmes, C. J. Obara, G. L. Martin, and C. S. Domack, "Manufacturing tolerances for natural laminar flow airframe surfaces," (1985), SAE Paper No. 850863.

[7] C. Obara and B. J. Holmes, "Flight-measured laminar boundary layer transition phenomena including stability theory analysis," (1985), NASA TP-2417.

[8] Y. X. Wang and M. Gaster, "Effect of surface steps on boundary layer transition," Exp. Fluids **39**, 679–686 (2005).

[9] M. Lessen and S. T. Gangwani, "Effect of small amplitude wall waviness upon the stability of the laminar boundary layer," Phys. Fluids **19**, 510–513 (1976).

[10] S. G. Lekoudis, A. H. Nayfeh, and W. C. Saric, "Compressible boundary layers over wavy walls," Phys. Fluids, **19**, 514–519 (1976).

[11] K. Kaups and T. Cebeci, "Compressible laminar boundary-layer with suction on swept and tapered wings," J. Aircraft **14**, 661–667 (1977).

[12] A. E. P. Veldman, "New quasi-simultaneous method to calculate interacting boundary layers," AIAA J. **19**, 79– (1981).

[13] A. H. Nayfeh, S. A. Ragab, and A. A. Al-Maalitah, "Effect of bulges on the stability of boundary layers," Phys. Fluids **31**, 796–806 (1988).

[14] T. Cebeci and D. A. Egan, "Prediction of transition due to isolated roughness," AIAA J. **27**, 870–875 (1989).

[15] J. A. Masad and V. Iyer, "Transition prediction and control in subsonic flow over a hump," Phys. Fluids **6**, 313–327 (1994).

[16] A. M. O. Smith and N. Gamberoni, "Transition, pressure gradient and stability theory," (1956), Douglas Airer. Co. Inc., ES 26388.

[17] J. L. Van Ingen, "A suggested semi-empirical method for the calculation of the boundary-layer transition region," (1956), Rep. Nos. VTH 71 and 74, Dept. Aeronaut. Eng., Univ. Technol., Delft, Neth.

[18] L. M. Mack, "Boundary-layer linear stability theory," (1984), AGARD Rep. No. 709, Von Kármán Inst., Rhode-St.-Genese, Belg.

[19] D. I. A. Poll, "Transition description and prediction in three-dimensional flows," (1984), AGARD Rep. No. 709, Von Kármán Inst., Rhode-St.-Genese, Belg.

[20] T-S. Wie and M. R. Malik, "Effect of surface waviness on boundary-layer transition in two-dimensional flow," Comp. Fluids **27**, 157–181 (1998).

[21] T. Herbert, "Parabolized stability equations," Annu. Rev. Fluid Mech. **29**, 245–283 (1997).

[22] J.-M. Lucas, O. Vermeersch, and D. Arnal, "Transient growth of gortler vortices in two-dimensional compressible boundary layers. application to surface waviness," Euro. J. Mech. B/Fluids **50**, 132–146 (2015).

[23] B. Gao, D. Park, and S. Park, "Stability analysis of a boundary layer over a hump using parabolized stability equations," Fluid Dyn. Res. **43**, 055503 (2011).

[24] D. Park and S. O. Park, "Linear and non-linear stability analysis of incompressible boundary layer over a two-dimensional hump," Comp. Fluids **73**, 80–96 (2013).

[25] C. Brehm, C. Koevary, T. Dackermann, and H. F. Fasel, "Numerical investigations of the influence of distributed roughness on Blasius boundary layer stability," AIAA Paper 2011-0563 (2011).

[26] M. Gaster, "Understanding the effects of surface roughness on the growth of disturbances," AIAA Paper 2016-4384 (2016).

[27] C. Thomas, S. M. Mughal, M. Gipon, R. Ashworth, and A. Martinez-Cava, "Stability of an infinite swept wing boundary layer with surface waviness," AIAA J. **50(10)**, 3024–3038 (2016).

[28] TAU, *Technical documentation of the DLR TAU-code release 2011.2.0. Institute of Aerodynamics and Flow Technology, Braunshweig.* (2011).

[29] S. M Mughal, "Stability analysis of complex wing geometries: Parabolised stability equations in generalised non-orthogonal coordinates," (2006), AIAA Paper 2006-3222, 2006. doi: 10.2514/6.2006-3222.

[30] S. M. Mughal and R. Ashworth, "Uncertainty quantification based receptivity modelling of crossflow instabilities induced by distributed surface roughness in swept wing boundary layers," (2013), AIAA Paper 2013-3106, 43rd AIAA Fluid Dynamics Conference, 2013. doi: 10.2514/6.2013-3106.

[31] M. R. Malik, "Hypersonic flight transition data analysis using parabolized stability equations with chemistry effects," J. Spacecraft Rockets **3**, 332–344 (2003).

[32] W. Liao, M. R. Malik, E. M. Lee-Rausch, F. Li, E. J. Nielsen, P. G. Buning, M. Choudhari, and C. Chang, "Boundary-layer stability analysis of the mean flows obtained using unstructured grids," J. Spacecraft Rockets **52**, 49–63 (2015).
[33] S. M. Mughal, "Transition prediction in fully 3d compressible flows," (2001), Imperial College London Final report prepared for QinetiQ and British Aerospace (MAD).
[34] M. Gaster, "The influence of surface roughness on boundary layer instability," AFOSR Review meeting, Dallas (2008).
[35] D. A. Hammond and L. G. Redekopp, "Local and global instability properties of separation bubbles," Euro. J. Mech. - B/Fluids **17**, 145–164 (1998).
[36] M. Alam and N. D. Sandham, "Direct numerical simulation of 'short' laminar separation bubbles with turbulent reattachment," J. Fluid Mech. **403**, 223–250 (2000).
[37] F. Li and M. R. Malik, "On the nature of the pse approximation," Theoret. Comput. Fluid Dyn **8**, 253–273 (1996).
[38] Y. C. Vignernon, J. V. Rakich, and J. C. Tannehill, "Calculation of supersonic viscous flow over delta wings with sharp subsonic leading edges," AIAA Paper 78–1337 (1978).
[39] P. Andersson, D. S. Henningson, and A. Hanifi, "On a stabilization procedure for the parabolic stability equations," J. Engng. Math. **33**, 311–332 (1998).
[40] P. R. Ashill, C. J. Beth, and M. Gaudet, "A wind tunnel study of transitional flows on a swept panel wing at high subsonic speeds," (1996), CEAS 2nd European forum on laminar flow technology.
[41] J. R. Edwards and S. Chandra, "Comparison of eddy-viscosity transport turbulence models for three-dimensional, shock separated flowfields," AIAA J. **34**, 756–763 (1996).
[42] U. Ayachit, "The paraview guide: A parallel visualization application," (2015), Kiteware, ISBN 978-1930934306.
[43] M. S. Mughal, "Active control of wave instabilities in three-dimensional compressible flows," Theoret. Comput. Fluid Dyn. **12**, 195–217 (1998).
[44] F. P. Bertolotti, Th. Herbert, and P. R. Spalart, "Linear and nonlinear stability of the Blasius boundary layer," J. Fluid Mech. **242**, 441–474 (1992).